# Gauging the Flexibility of the Active Site in Soybean Lipoxygenase-1 (SLO-1) through an Atom-Centered Density Matrix Propagation (ADMP) Treatment That Facilitates the Sampling of Rare Events

Prasad Phatak, Isaiah Sumner, and Srinivasan S. Iyengar*

Department of Chemistry and Department of Physics, Indiana University, 800 East Kirkwood Avenue, Bloomington, Indiana 47405, United States

Ⓢ Supporting Information

ABSTRACT: We present a computational methodology to sample rare events in large biological enzymes that may involve electronically polarizing, reactive processes. The approach includes simultaneous dynamical treatment of electronic and nuclear degrees of freedom, where contributions from the electronic portion are computed using hybrid density functional theory and the computational costs are reduced through a hybrid quantum mechanics/molecular mechanics (QM/MM) treatment. Thus, the paper involves a QM/MM dynamical treatment of rare events. The method is applied to probe the effect of the active site elements on the critical hydrogen transfer step in the soybean lipoxygenase-1 (SLO-1) catalyzed oxidation of linoleic acid. It is found that the dynamical fluctuations and associated flexibility of the active site are critical toward maintaining the electrostatics in the regime where the reactive process can occur smoothly. Physical constraints enforced to limit the active site flexibility are akin to mutations and, in the cases studied, have a detrimental effect on the electrostatic fluctuations, thus adversely affecting the hydrogen transfer process.
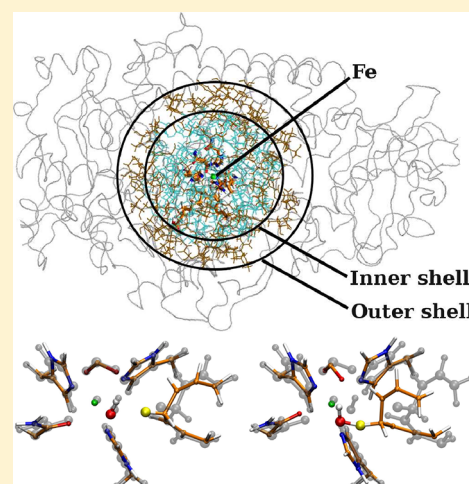
I. INTRODUCTION

Chemical processes in biological systems generally occur over a range of time-scales that span several orders of magnitude. For example, hydrogen transfer[1−3] in an enzyme complex can occur on the order of femto- to picoseconds. While these shorter time-scales can be studied using *ab initio* molecular dynamics (AIMD) methods,[4−16] the time-scales for protein structural rearrangements that facilitate proton transfer processes transpire over the micro- to millisecond time-scales,[17−24] which are inaccessible to AIMD. For classical molecular dynamics studies using parametrized force-fields, several approximate coarse-graining techniques have been developed to sample rare events.[25−32] Nevertheless, challenges remain, particularly for cases where (a) explicit treatment of electronic and (b) quantum-mechanical treatment of nuclear degrees of freedom are necessary. A combination of these effects generally plays a critical role in the detailed study of hydrogen transfer reactions in several enzymes.[20,21,23,24,33−42]

In this study, we focus on the development of an approach for rare events sampling that retains electronic structural components during dynamics. While the problems studied in this paper involve classical treatment of nuclei, the approach lends itself naturally to a quantum-nuclear generalization which will be evaluated and benchmarked in future publications. The methods proposed here are influenced by several approaches to obtain biased dynamics trajectories. Some of these approaches

are briefly reviewed here. The paragraph below is by no means exhaustive and is only included to draw the connections between our approach and other well-known techniques.

One family of methods[27,43−52] that compute biased classical trajectories to sample rare events includes the introduction of fictitious, "bath-like" degrees of freedom. The choice of the bath-related parameters, such as bath-inertia, initial conditions, and the coupling potential between the bath and molecular degrees of freedom, are critical, since these: (a) determine the sampling involved for the molecular degrees of freedom and (b) place bounds on the extent to which the molecular system Hamiltonian is perturbed. Such approaches have been combined[53−55] with extended Lagrangian techniques[56−59] for (a) schemes that allow efficient treatment of systems having a large separation in time-scales[60−64] and (b) simulations of other ensembles.[56−59] Another example of extended Lagrangian techniques is a growing class of strategies that allow the inclusion of electronic degrees of freedom with nuclear (classical and quantum) dynamics in real[65−67] and imaginary[68−73] time. Direct variational minimization of action to obtain long time-scale classical trajectories that sample rare events is another approach that was introduced by Elber and co-workers.[74−78] This approach was further extended by

Parrinello to include electronic structure.[79,80] In Chandler's transition path sampling,[18,81] a precomputed path that connects two potential wells is refined through a Monte Carlo procedure with sampling based on the classical action. This leads to an ensemble of productive trajectories (transition path ensemble). Several other groups have developed an approach along a similar vein.[82−84] In addition, another common approach is to create biased ensembles[50,85,86] (i.e., bias the initial conditions) or to bias the potential energy surface[87,88] to increase the likelihood of sampling a rare event. These schemes rely on the ability to then determine experimental observables such as rate constants based on the unbiased, experimental conditions.[49] Sampling rare events also plays a predominant role in the construction of free energy surfaces.[27,43−50,89−91] A prime example is Jarzynski's equality (JE),[43−45] which relates non-equilibrium work, obtained through a bias potential, to the change in free energy.

In this publication, we introduce a simple rare events sampling methodology. The approach is discussed in section II for classical dynamical treatment of nuclei. Numerical benchmarks on the method are provided in Appendix A. The method is used to probe the role of active site groups, specifically those bound to the iron cofactor in soybean lipoxygenase-1 (SLO-1). In this regard, a QM/MM[6,8,10,12−14,92−95,95−107] generalization of the rare events sampling methodology is employed and also discussed in section IIA. Further benchmarks relating to these QM/MM simulations on SLO-1 are provided as part of the Supporting Information. The results are discussed in section III, and these are supplemented by detailed calculations that are discussed in Appendix B. Conclusions are given in section IV.

II. RARE-EVENTS SAMPLING BASED ON *AB INITIO* MOLECULAR DYNAMICS

The approach outlined in this section is similar to the fictitious (bath) particle methods outlined in the Introduction. We couple a family of "bath variables", denoted through positions $\tilde{\mathbf{R}}$, to a chosen set of nuclear degrees of freedom via a coupling potential. We also assign inertia to the fictitious degrees of freedom which allows us to define associated momenta. To simultaneously treat electronic and nuclear degrees of freedom, we begin with a modified extended Lagrangian atom-centered density-matrix propagation (ADMP) description:[6,61,108−122]

$$\mathcal{L} = \frac{1}{2}Tr[\mathbf{V^T MV}] + \frac{1}{2}Tr([\mu^{1/4}\mathbf{W}\mu^{1/4}]^2) + \frac{1}{2}Tr[\mathbf{\tilde{V}^T \tilde{M}\tilde{V}}]$$
$$- E(\mathbf{R}, \mathbf{P}) - \eta(\mathbf{R}; \tilde{\mathbf{R}}) - Tr[\mathbf{\Lambda}(\mathbf{PP} - \mathbf{P})] \quad (1)$$

where $\mathbf{M}$, $\mathbf{R}$, and $\mathbf{V}$ are the nuclear masses, atomic positions, and velocities. The quantities $\tilde{\mathbf{M}}$, $\tilde{\mathbf{R}}$, and $\hat{\mathbf{V}}$ are the masses, positions, and velocities of the family of fictitious, bath particles, and the function $E(\mathbf{R}, \mathbf{P})$ is the *ab initio* potential energy function. This potential energy is a function of the single-particle electronic density matrix, $\mathbf{P}$, and nuclear positions, $\mathbf{R}$. In this work, a QM/MM description is used for $E(\mathbf{R}, \mathbf{P})$ and discussed in section IIA. The electronic density matrix, density matrix velocity, and fictitious inertia tensor[108] for the electronic degrees of freedom are $\mathbf{P}$, $\mathbf{W}$, and μ, respectively. The last term in eq 1 imposes constraints on the total number of electrons and on the idempotency of the density matrix using a Lagrangian multiplier matrix $\mathbf{\Lambda}$. The function $\eta(\mathbf{R}; \tilde{\mathbf{R}})$ is a coupling or tethering constraint on $\mathbf{R}$ through introduction of $\tilde{\mathbf{R}}$, and the function also defines the subset of particles in $\mathbf{R}$ that are influenced by

the constraint. In this study, we employ a harmonic tethering constraint and hence the extended Lagrangian used here is

$$\mathcal{L} = \frac{1}{2}Tr[\mathbf{V^T MV}] + \frac{1}{2}Tr([\mu^{1/4}\mathbf{W}\mu^{1/4}]^2) + \frac{1}{2}Tr[\mathbf{\tilde{V}^T \tilde{M}\tilde{V}}]$$
$$- E(\mathbf{R}, \mathbf{P}) - \frac{1}{2}Tr[(\mathbf{R} - \tilde{\mathbf{R}})^T \mathbf{K}(\mathbf{R} - \tilde{\mathbf{R}})]$$
$$- Tr[\mathbf{\Lambda}(\mathbf{PP} - \mathbf{P})] \quad (2)$$

where $\mathbf{K}$ is a *positive-definite* harmonic force constant matrix. When chosen to be a full-matrix, $\mathbf{K}$ may also include a coordinate transformation. However, in this study, $\mathbf{K}$ is chosen to be diagonal in the molecular coordinate frame.

The Euler−Lagrange equations of motion are

$$\mathbf{M}\frac{d^2\mathbf{R}}{dt^2} = -\frac{\partial E(\mathbf{R}, \mathbf{P})}{\partial \mathbf{R}}\bigg|_P - \frac{1}{2}[(\mathbf{R} - \tilde{\mathbf{R}})^T \mathbf{K} + \mathbf{K}(\mathbf{R} - \tilde{\mathbf{R}})] \quad (3)$$

$$\tilde{\mathbf{M}}\frac{d^2\tilde{\mathbf{R}}}{dt^2} = \frac{1}{2}[(\mathbf{R} - \tilde{\mathbf{R}})^T \mathbf{K} + \mathbf{K}(\mathbf{R} - \tilde{\mathbf{R}})] \quad (4)$$

$$\mu^{1/2}\frac{d^2\mathbf{P}}{dt^2}\mu^{1/2} = -\frac{\partial E(\mathbf{R}, \mathbf{P})}{\partial \mathbf{P}}\bigg|_R - \mathbf{\Lambda P} - \mathbf{P\Lambda} + \mathbf{\Lambda} \quad (5)$$

These are integrated using the velocity Verlet scheme.[123] Since the force on the classical particles (first term on right side of eq 3) is augmented by additional forces from $\tilde{\mathbf{R}}$ (second term on right side of eq 3), the dynamics of $\tilde{\mathbf{R}}$ are utilized to bias the dynamics of the nuclei. In this way, our trajectories may access regions in phase space that are not readily sampled during the normal course of AIMD. In regards to the extended Lagrangian in eq 1, see also ref 67, where this Lagrangian has been generalized to include multiple diabatic states and their influence on quantum nuclear dynamics. It must also be noted that the electronic gradients in eq 3, $(\partial E(\mathbf{R}, \mathbf{P})/\partial \mathbf{R})|\mathrm{BF_P}$, are more general than those in standard Born−Oppenheimer dynamics[61,110] on account of the non-negligible magnitude of the commutator of the Fock and density matrix. See refs 61, 110, 121, and 122.

A. The Hybrid Energy Functional, *E*(R, P), Constructed through the ONIOM Scheme. The simulations were carried out using a hybrid quantum mechanics/molecular mechanics (QM/MM) generalization of ADMP.[6] Here, the energy functional, $E(\mathbf{R}, \mathbf{P})$, in eq 1 is modified according to

$$E(\mathbf{R}, \mathbf{P}) \rightarrow E_{n\text{-layer}}^{\text{ONIOM}}(\mathbf{R})$$
$$= \sum_{i=2}^{n,(n\geq2)} S_{(i);(i-1)}^{i}(\mathbf{R}; \mathbf{P}_{\text{system},i}^{\text{level},i}, \mathbf{P}_{\text{system},i-1}^{\text{level},i})$$
$$+ E_{\text{system},1}^{\text{level},1}(\mathbf{R}; \mathbf{P}_{\text{system},1}^{\text{level},1}) \quad (6)$$

where the ONIOM extrapolation term is

$$S_{(i);(i-1)}^{i}(\mathbf{R}; \mathbf{P}_{\text{system},i}^{\text{level},i}, \mathbf{P}_{\text{system},i-1}^{\text{level},i})$$
$$= E_{\text{system},i}^{\text{level},i}(\mathbf{R}, \mathbf{P}_{\text{system},i}^{\text{level},i}) - E_{\text{system},i-1}^{\text{level},i}(\mathbf{R}, \mathbf{P}_{\text{system},i-1}^{\text{level},i}) \quad (7)$$

The system size increases and the calculation level decreases from i to $i + 1$. Each layer is treated at two levels (i and $i − 1$), while the entire system is only considered at the lowest level (n). If chemical bonds intersect the boundary between two layers, link atoms are used to saturate the dangling valencies of the smaller system.[124] The positions of link atoms are uniquely

determined on the basis of the connectivity of the system, which makes conservative Hamiltonian dynamics possible.[6] Thus, the selected atoms and additional link atoms of each system are influenced by the properties of the atoms in the larger systems.

In this study, the layers of ONIOM are coupled through mechanical embedding.[125] In mechanical embedding, the smaller system calculations are performed in the absence of the larger system atoms. Here, only the link atoms are directly influenced by the larger system and their placement is constrained by the positions of the substituted atoms in the larger system. An essential ingredient of the formalism is the fact that the correct number of degrees of freedom are maintained in the overall potential energy functions; the unique definition of the potential energy is ensured by defining the coordinates of the link atom as[126−128]

$$\mathbf{r}_{link} = \mathbf{r}_{bond} + g(\mathbf{r}_{sub} - \mathbf{r}_{bond}) \qquad (8)$$

where $\mathbf{r}_{bond}$ is the position of the atom to which the link atom is bound in the smaller system (for example, the system labeled as i) and $\mathbf{r}_{sub}$ belongs to the surrounding (for example, the system labeled as $i + 1$). The quantity g is a predefined scaling factor. Clearly, using this expression, $\mathbf{r}_{link}$ can be eliminated from the potential energy function and energy gradients, as these can be written in terms of $\mathbf{r}_{bond}$ and $\mathbf{r}_{sub}$ using the above expression.

For the QM portion of the above expression, the energy, $E(\mathbf{R}, \mathbf{P})$, is calculated using McWeeny purification,[129] $\tilde{\mathbf{P}} = 3\mathbf{P}^2 - 2\mathbf{P}^3$:

$$E = Tr\left[\mathbf{h}'\tilde{\mathbf{P}}' + \frac{1}{2}\mathbf{G}'(\tilde{\mathbf{P}}')\tilde{\mathbf{P}}'\right] + E_{xc} + V_{NN}$$

$$= Tr\left[\mathbf{h}\tilde{\mathbf{P}} + \frac{1}{2}\mathbf{G}(\tilde{\mathbf{P}})\tilde{\mathbf{P}}\right] + E_{xc} + V_{NN} \qquad (9)$$

Here, $\mathbf{h}'$ is the one electron matrix in the non-orthogonal Gaussian basis and $\mathbf{G}'(\tilde{\mathbf{P}}')$ is the two electron matrix for Hartree−Fock calculations, but for density functional calculations, it represents the Coulomb potential. The term E_{xc} is the DFT exchange-correlation functional (for Hartree−Fock, $E_{xc} = 0$), while V_{NN} represents the nuclear repulsion energy. In the orthonormal basis, these matrices are $\mathbf{h} = \mathbf{U}^{-T}\mathbf{h}'\mathbf{U}^{-1}$, etc., where the overlap matrix for the non-orthogonal Gaussian basis, $\mathbf{S}'$, is factorized to yield $\mathbf{S}' = \mathbf{U}^T\mathbf{U}$. There are a number of choices for the transformation matrix $\mathbf{U}$; e.g., $\mathbf{U}$ can be obtained from Cholesky decomposition[130] of $\mathbf{S}'$ or $\mathbf{U} = \mathbf{S}'^{1/2}$ for Löwdin symmetric orthogonalization.[131] The matrix $\mathbf{U}$ can also include an additional transformation so that overall rotation of the system is factored out of the propagation of the density. The density matrix in the orthonormal basis, $\mathbf{P}$, is related to the density matrix in the non-orthogonal Gaussian basis, $\mathbf{P}'$, by $\mathbf{P} \equiv \mathbf{U}\mathbf{P}'\mathbf{U}^T$. The QM/MM expression discussed above utilizes the orthonormal basis representation of the density matrix.

Although the above discussion is general for any partitioning scheme (n-layer ONIOM), the present work uses a 2-layer implementation, i.e., ONIOM(MO:MM) (SCF (b3lyp/lanl2dz) and molecular mechanics (Dreiding[132,133] and CHARMM)) with mechanical embedding. In this case, the energy expressions, eqs 6 and 7, reduce to

$$E(\mathbf{R}, \mathbf{P}) \rightarrow E_{2\text{-layer}}^{ONIOM}(\mathbf{R})$$

$$= E_{system,2}^{level,2}(\mathbf{R}, \mathbf{P}_{system,2}^{level,2}) - E_{system,1}^{level,2}(\mathbf{R}, \mathbf{P}_{system,1}^{level,2})$$

$$+ E_{system,1}^{level,1}(\mathbf{R}; \mathbf{P}_{system,1}^{level,1}) \qquad (10)$$

Here, system,1 is generally referred to as the *real* system, whereas system,2 is referred to as the *model*, and consequently the commonly utilized MO/MM expression[134] is

$$E(\mathbf{R}, \mathbf{P}) \rightarrow E^{IMOMM}(\mathbf{R}) = E_{real}^{MM} - E_{model}^{MM} + E_{model}^{QM} \qquad (11)$$

When the above functional forms of energy are implemented within the ADMP scheme (eq 1), the following advantages arise. ADMP can be applied using accurate QM models, including hybrid density functional theory (DFT), as well as more advanced functionals that utilize the kinetic energy density.[135−137] This is particularly important for studies of reactivity in biological systems, because semi-empirical methods and pure density functionals have limited accuracy for transition state structures and reaction paths, especially when transition metals are involved. Another crucial issue when hybrid methods are employed to treat large systems is the computational efficiency. The ADMP/ONIOM approach shows an asymptotic O(N) scaling by virtue of established techniques[138] and the capability of employing reasonably large time-steps through the use of a tensorial fictitious mass.[108] Finally, ADMP allows one to treat all electrons in the QM region of the system explicitly without resorting to pseudopotentials (unless so desired), and to systematically control the deviation from the Born−Oppenheimer surface.[110]

A QM/QM multilayer implementation of ADMP is currently in progress. All calculations are performed using a developmental version of the Gaussian series of electronic structure programs.[139]

B. Analysis of the Lagrangian in eqs 1 and 2. To probe the effect of the "bath" variables, $\tilde{\mathbf{R}}$, as well as the effect of the constraint potential, $\eta(\mathbf{R}; \tilde{\mathbf{R}})$, we introduce the conjugate Hamiltonian, given by the Legendre transform[140] of the Lagrangian:

$$\mathcal{H}(\mathbf{P}, \mathcal{W}, \mathbf{R}, \mathcal{V}, \tilde{\mathbf{R}}, \tilde{\mathcal{V}}, \mathbf{t})$$

$$= \mathbf{Tr}(\mathcal{W}\mathbf{W}) + \mathbf{Tr}(\mathcal{V}^{\mathbf{T}}\mathbf{V}) + \mathbf{Tr}(\tilde{\mathcal{V}}^{\mathbf{T}}\tilde{\mathbf{V}})$$

$$- \mathcal{L}(\mathbf{P}, \mathbf{W}, \mathbf{R}, \mathbf{V}, \tilde{\mathbf{R}}, \tilde{\mathbf{V}}, \mathbf{t}) \qquad (12)$$

where $\mathcal{W}$, $\mathcal{V}$, and $\tilde{\mathcal{V}}$ are the conjugate momenta for $\mathbf{P}$, $\mathbf{R}$, and $\tilde{\mathbf{R}}$, respectively, and are given by

$$\mathcal{W} = \frac{\partial \mathcal{L}}{\partial \mathbf{W}} = \mu^{1/2}\mathbf{W}\mu^{1/2} \qquad (13)$$

$$\mathcal{V} = \frac{\partial \mathcal{L}}{\partial \mathbf{V}} = \mathbf{MV} \qquad (14)$$

and

$$\tilde{\mathcal{V}} = \frac{\partial \mathcal{L}}{\partial \tilde{\mathbf{V}}} = \tilde{\mathbf{M}}\tilde{\mathbf{V}} \qquad (15)$$

Using eqs 13−15 in eq 12, one obtains the conjugate Hamiltonian as

$$\mathcal{H} = \frac{1}{2}Tr(\mathcal{V}^{\mathbf{T}}\mathbf{M}^{-1}\mathcal{V}) + \frac{1}{2}Tr(\tilde{\mathcal{V}}^{\mathbf{T}}\mathbf{M}^{-1}\tilde{\mathcal{V}})$$

$$+ \frac{1}{2}Tr(\mathcal{W}\mu^{-1/2}\mathcal{W}\mu^{-1/2}) + E(\mathbf{R}, \mathbf{P}) + \eta(\mathbf{R}; \tilde{\mathbf{R}})$$

$$+ Tr[\mathbf{\Lambda}(\mathbf{PP} - \mathbf{P})] \qquad (16)$$

or

$$\mathcal{H} = \frac{1}{2} Tr(\mathcal{V}^{\mathbf{T}} \mathbf{M}^{-1} \mathcal{V}) + \frac{1}{2} Tr(\tilde{\mathcal{V}}^{\mathbf{T}} \mathbf{M}^{-1} \tilde{\mathcal{V}})$$
$$+ \frac{1}{2} Tr(\mathcal{W} \mu^{-1/2} \mathcal{W} \mu^{-1/2}) + E(\mathbf{R}, \mathbf{P})$$
$$+ \frac{1}{2} Tr[(\mathbf{R} - \tilde{\mathbf{R}})^{\mathbf{T}} \mathbf{K} (\mathbf{R} - \tilde{\mathbf{R}})] + Tr[\mathbf{\Lambda}(\mathbf{PP} - \mathbf{P})] \tag{17}$$

We may partition the above Hamiltonian as a system-bath Hamiltonian with definitions

$$\mathcal{H}_{\text{system}} = \frac{1}{2} Tr(\mathcal{V}^{\mathbf{T}} \mathbf{M}^{-1} \mathcal{V}) + \frac{1}{2} Tr(\mathcal{W} \mu^{-1/2} \mathcal{W} \mu^{-1/2})$$
$$+ E(\mathbf{R}, \mathbf{P}) + Tr[\mathbf{\Lambda}(\mathbf{PP} - \mathbf{P})] \tag{18}$$

and

$$\mathcal{H}_{\text{bath}} = \frac{1}{2} Tr(\tilde{\mathcal{V}}^{\mathbf{T}} \mathbf{M}^{-1} \tilde{\mathcal{V}}) + \eta(\mathbf{R}; \tilde{\mathbf{R}}) \tag{19}$$

so that

$$\mathcal{H} = \mathcal{H}_{\text{system}} + \mathcal{H}_{\text{bath}} \tag{20}$$

Clearly, the goal is to couple a subset of particles in $\mathbf{R}$ to the bath defined by $\mathcal{H}_{\text{bath}}$ in order to nudge the dynamics in the direction of the rare event in question.

To investigate the conservation property for the above Hamiltonian, we consider the total derivative of $\mathcal{H}$ with respect to t:

$$\frac{d\mathcal{H}}{dt} = Tr\left[\frac{\partial\mathcal{H}}{\partial\mathbf{P}} \frac{d\mathbf{P}}{dt} + \frac{\partial\mathcal{H}}{\partial\mathcal{W}} \frac{d\mathcal{W}}{dt} + \frac{\partial\mathcal{H}}{\partial\mathbf{R}} \frac{d\mathbf{R}}{dt} + \frac{\partial\mathcal{H}}{\partial\mathcal{V}} \frac{d\mathcal{V}}{dt} \right.$$
$$\left. + \frac{\partial\mathcal{H}}{\partial\tilde{\mathbf{R}}} \frac{d\tilde{\mathbf{R}}}{dt} + \frac{\partial\mathcal{H}}{\partial\tilde{\mathcal{V}}} \frac{d\tilde{\mathcal{V}}}{dt} \right]$$
$$= \left\{ Tr\left[\left(\frac{\partial E(\mathbf{R}, \mathbf{P})}{\partial\mathbf{P}} \Big|_{\mathbf{R}} + \mathbf{\Lambda P} + \mathbf{P\Lambda} - \mathbf{\Lambda} \right) \mathcal{W} \right] \right.$$
$$\left. + Tr\left[\mathcal{W} \frac{d^2\mathbf{P}}{dt^2} \right] \right\} + \left\{ Tr\left[\left(\frac{\partial E(\mathbf{R}, \mathbf{P})}{\partial\mathbf{R}} \Big|_{\mathbf{P}} + \frac{\partial\eta}{\partial\mathbf{R}} \right) \mathcal{V} \right] \right.$$
$$\left. + Tr\left[\mathcal{V} \frac{d^2\mathbf{R}}{dt^2} \right] \right\} + \left\{ Tr\left[\frac{\partial\eta}{\partial\tilde{\mathbf{R}}} \tilde{\mathcal{V}} \right] + Tr\left[\tilde{\mathcal{V}} \frac{d^2\tilde{\mathbf{R}}}{dt^2} \right] \right\} \tag{21}$$

where the definitions in eqs 13–15 are used and it is assumed that μ is time independent. For the case where $\eta(\mathbf{R}; \tilde{\mathbf{R}}) \equiv \frac{1}{2} Tr[(\mathbf{R} - \tilde{\mathbf{R}})^{\mathbf{T}} \mathbf{K} (\mathbf{R} - \tilde{\mathbf{R}})]$

$$-\frac{\partial\eta}{\partial\tilde{\mathbf{R}}} \equiv \frac{\partial\eta}{\partial\mathbf{R}} = \left(\frac{1}{2} (\mathbf{R} - \tilde{\mathbf{R}})^{\mathbf{T}} \mathbf{K} + \frac{1}{2} \mathbf{K} (\mathbf{R} - \tilde{\mathbf{R}}) \right) \tag{22}$$

Using the Euler−Lagrange equations of motion, i.e., eqs 3−5, it may be noted that the terms inside each curly bracket, {...}, in eq 21 are independently equal to zero and hence

$$\frac{d\mathcal{H}}{dt} = 0 \tag{23}$$

Therefore, the Hamiltonian in eq 17 represents a conservative system.

Bounds on fluctuations in $\mathcal{H}_{\text{system}}$ and $\mathcal{H}_{\text{bath}}$ can also be derived as follows. Since $\mathcal{H} \equiv \mathcal{H}_{\text{system}} + \mathcal{H}_{\text{bath}}$, for the case where $\eta(\mathbf{R}; \tilde{\mathbf{R}}) \equiv \frac{1}{2} Tr[(\mathbf{R} - \tilde{\mathbf{R}})^{\mathbf{T}} \mathbf{K} (\mathbf{R} - \tilde{\mathbf{R}})]$:

$$\frac{d\mathcal{H}_{\text{bath}}}{dt} = -\frac{d\mathcal{H}_{\text{system}}}{dt} = Tr\left[\frac{\partial\mathcal{H}_{\text{bath}}}{\partial\mathbf{R}} \frac{d\mathbf{R}}{dt} + \frac{\partial\mathcal{H}_{\text{bath}}}{\partial\tilde{\mathbf{R}}} \frac{d\tilde{\mathbf{R}}}{dt} \right.$$
$$\left. + \frac{\partial\mathcal{H}_{\text{bath}}}{\partial\tilde{\mathcal{V}}} \frac{d\tilde{\mathcal{V}}}{dt} \right]$$
$$= \left\{ Tr\left[\left(\frac{1}{2} (\mathbf{R} - \tilde{\mathbf{R}})^{\mathbf{T}} \mathbf{K} + \frac{1}{2} \mathbf{K} (\mathbf{R} - \tilde{\mathbf{R}}) \right) \mathcal{V} \right] \right\}$$
$$+ \left\{ -Tr\left[\left(\frac{1}{2} (\mathbf{R} - \tilde{\mathbf{R}})^{\mathbf{T}} \mathbf{K} + \frac{1}{2} \mathbf{K} (\mathbf{R} - \tilde{\mathbf{R}}) \right) \tilde{\mathcal{V}} \right] \right.$$
$$\left. + Tr\left[\tilde{\mathcal{V}} \frac{d^2\tilde{\mathbf{R}}}{dt^2} \right] \right\}$$
$$= Tr\left[\left(\frac{1}{2} (\mathbf{R} - \tilde{\mathbf{R}})^{\mathbf{T}} \mathbf{K} + \frac{1}{2} \mathbf{K} (\mathbf{R} - \tilde{\mathbf{R}}) \right) \mathcal{V} \right]$$
$$\equiv Tr\left[\frac{\partial\eta}{\partial\mathbf{R}} \mathcal{V} \right] \tag{24}$$

Thus, the bath Hamiltonian fluctuations are determined by fluctuations in the constraint term as well as the velocities of the particles in the system. The constraint term is to be chosen so as to provide a driving force for the system to scale a transition barrier. Additional requirements on the constraint term are given in Appendix A and section IIIB.

Molecular dynamics trajectories constructed using eqs 3−5 provide ensemble averages where the phase space is weighted according to $[\exp(-\beta\mathcal{H})/Q_{\mathcal{H}}]$. Here, $Q_{\mathcal{H}}$ is the partition function constructed from $\mathcal{H}$ and $\beta \equiv 1/(k_B T)$ is the inverse temperature. To obtain the appropriate values consistent with $\mathcal{H}_{\text{system}}$, i.e., weighted according to $[\exp(-\beta\mathcal{H}_{\text{system}})/Q_{\mathcal{H}\,\text{system}}]$, one needs to construct the averages for observables defined as $[A \exp(+\beta\eta)]$, while monitoring the quantity $\exp(+\beta\eta)$ during the dynamics to provide the appropriate normalization, and obtain ensemble averages for the property A. In other words,

$$\langle A \rangle_{\mathcal{H}_{\text{system}}} \equiv \frac{\int d\Gamma_{\text{system}} A \exp(-\beta\mathcal{H}_{\text{system}})}{\int d\Gamma_{\text{system}} \exp(-\beta\mathcal{H}_{\text{system}})}$$
$$= \frac{\int d\Gamma_{\text{system}} A \exp(+\beta\mathcal{H}_{\text{bath}}) \exp(-\beta\mathcal{H})}{\int d\Gamma_{\text{system}} \exp(+\beta\mathcal{H}_{\text{bath}}) \exp(-\beta\mathcal{H})}$$
$$= \frac{\langle A \exp(+\beta\eta) \rangle'_{\mathcal{H}}}{\langle \exp(+\beta\eta) \rangle'_{\mathcal{H}}} \tag{25}$$

where Γ_{system} includes the position and momenta in $\mathcal{H}_{\text{system}}$ (see eq 18) and the superscript prime in the last equation indicates that, while the ensemble averages are constructed from $\mathcal{H}$ (the subscripts therein), the integration is over the phase space of $\mathcal{H}_{\text{system}}$ and not $\mathcal{H}$. For sampling issues that arise from such a biased dynamics formalism, please see refs 50 and 51. In section III, the biased ADMP formalism introduced here is utilized to gauge the effect of the active site components on the hydrogen transfer process in soybean lipoxygenase-1 (SLO-1).

It is useful to compare the Hamiltonian in eq 16 with the reaction path Hamiltonian (RPH) derived by Miller and co-workers.[141]
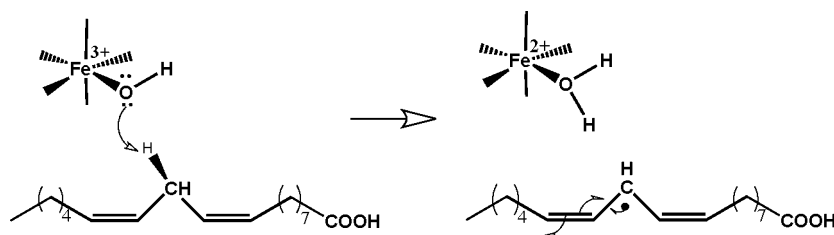
Figure 1. Hydrogen abstraction is the rate determining step in the oxidation of linoleic acid by SLO-1.

In the case of RPH, a $(3N - 6)$-dimensional Hamiltonian is constructed, where $3N - 7$ degrees of freedom are treated using the harmonic approximation, with frequencies determined from the curvature of the potential surface, and the remaining reaction coordinate momentum is corrected by projecting out a coupling element between the harmonic normal modes:

$$
\begin{aligned}
& H(p_s, s, \{P_k, Q_k\}) \\
&= \sum_{k=1}^{3N-7} \left(\frac{1}{2} P_k^2 + \frac{1}{2} \omega_k^2(s) Q_k^2 \right) + V_0(s) \\
&\quad + \frac{1}{2} \frac{[p_s - \sum_{k,l=1}^{3N-7} Q_k P_l B_{k,l}(s)]^2}{[1 + \sum_{k=1}^{3N-7} Q_k B_{k,3N-6}(s)]^2}
\end{aligned}
\tag{26}
$$

Here, the reaction coordinate s is the arc length along the reaction path with value zero at the transition state and p_s is its conjugate momentum. $\{Q_k\}$ represent normal coordinates for vibrations with corresponding conjugate momenta $\{P_k\}$ for $k = 1, ..., 3N - 7$. The quantity s is the $(3N - 6)$th degree of freedom, and $B_{k,l}(s)$ is the coupling between kth and lth vibrational modes.

Dynamics using this RPH Hamiltonian results in trajectories along the transition path, where the orthogonal dimensions are purely harmonic. This may be contrasted with the Hamiltonian in eq 16 where the potential, $E(\mathbf{R}, \mathbf{P})$, is determined from instantaneous electronic structure calculations and no quadratic approximation is invoked during dynamics for any of the degrees of freedom. That is,

$$
\begin{aligned}
& \frac{1}{2} \omega_k^2(s) Q_k^2 + V_0(s) + \left\{ \frac{1}{2} \frac{[p_s - \sum_{k,l=1}^{3N-7} Q_k P_l B_{k,l}(s)]^2}{[1 + \sum_{k=1}^{3N-7} Q_k B_{k,3N-6}(s)]^2} \right. \\
&\quad \left. - \frac{p_s^2}{2} \right\} \rightarrow E(\mathbf{R}, \mathbf{P}) + \eta(\mathbf{R}; \tilde{\mathbf{R}}) + Tr[\mathbf{\Lambda}(\mathbf{PP} - \mathbf{P})]
\end{aligned}
\tag{27}
$$

as a correspondence between eqs 26 and 16. Furthermore, since the Hamiltonian in eq 26 involves $3N - 6$ dimensions, there is no rotation−vibration coupling involved. By contrast, the Hamiltonian in eq 16 is constructed in $3N$ space. This is also clear from eq 27 where the left side has $3N - 6$ degrees of freedom, whereas the right side has $3N$ degrees of freedom. The bath Hamiltonian, $\mathcal{H}_{bath}$, defined in eq 19 constitutes an external field introduced to drive the transition for the case of the Hamiltonian in eq 16.

Numerical benchmarks on the rare events sampling methodology are provided in Appendix A.

III. SIMULATIONS ON SOYBEAN LIPOXYGENASE-1 (SLO-1) USING THE ADMP-BASED RARE-EVENTS SAMPLING APPROACH

Enzymes play a significant role in biochemical reactions[142] due to their ability to achieve high reaction rates[143] through catalysis. Despite dedicated efforts,[144,142] probing mechanisms and routes through which enzymes accelerate reactions remains a major challenge[35,145,146] in biochemistry. A significant number of experimental as well as theoretical studies have focused on understanding the connections between the enzyme structure, dynamics, and function.[147−155] In recent years, hydrogen tunneling has also been thought to play a significant role in enzyme kinetics.[15−17,20,21,34−36,42,156−158] Of particular interest is an enzyme, soybean lipoxygenase-1 (SLO-1), that has become a prototype for studying hydrogen tunneling in enzyme catalysis. SLO-1 is an oxygen-dependent non-heme iron enzyme that catalyzes the oxidation of linoleic acid (LA)[23,24,38−42,159−162] In mammals, lipoxygenase catalyzes the production of leukotrienes and lipoxin and plays an important role in inflammatory responses.[163,164] It has been shown that inhibition of this enzyme inhibits tumor-genesis and lipoxygenase has been proposed as a promising cancer chemo-preventive agent.[163,164] The rate-determining step in the catalytic cycle is the abstraction of a hydrogen atom from the fatty acid chain by the octahedral $Fe^{3+}-OH$ active site complex (see Figure 1). This is followed by a radical attack by O_2 that results in the final peroxide complex.[162] The rate determining step displays a large primary kinetic isotope effect ($k_H/k_D = 81$) at room temperature under certain mutations,[165] and also displays a weak temperature dependence of the reaction rate constant.[37,39,159,165]

In ref 7, we explored the quantum dynamical nature of the hydrogen/deuterium nuclear transfer process involved in the rate-determining step in the catalytic cycle of the enzyme SLO-1 (Figure 1). We computed the hydrogen tunneling probabilities for a model system constructed from the active site atoms in close proximity to the iron cofactor in SLO-1. This simplification of the active site is based on the assumption that only the immediate environment exerts an electronic influence on the hydrogen nuclear transfer. We described the tunneling hydrogen nucleus (proton or deuteron) as a three-dimensional nuclear quantum wavepacket[7,8,166−169] coupled to the change in electronic structure which was computed using hybrid density functional theory, benchmarked through MP2 post-Hartree−Fock calculations. At each step of the quantum dynamics, the potential surface was computed by *including all electrons* in our model system. As a result, the method in ref 7 is not restricted to a specific mode of transfer such as proton coupled electron transfer,[41,170] proton transfer, hydrogen transfer, or hydride transfer. In addition, the transferring nuclear wavepacket is propagated via the time-dependent Schrödinger equation, using an efficient and accurate
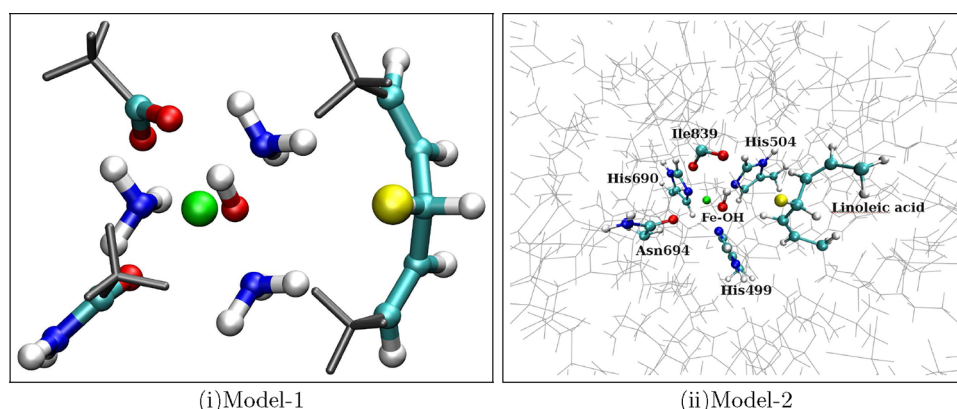
(i)Model-1   (ii)Model-2

Figure 2. The two active site model systems used for the AIMD simulation of rare events. (i) Model-1 contains 50 atoms and is similar to that used in refs 7 and 9. (ii) Model-2 is treated using a QM/MM description. (See the Supporting Information for a discussion on the asymptotic boundary conditions used to obtain the dynamical subset of 2174 atoms shown here.) The color codes for the QM region (shown using a CPK representation) are as follows: carbon (cyan), hydrogen (white), oxygen (red), nitrogen (blue), iron (green), and the transferring pro-S hydrogen is represented in yellow. The remaining atoms shown in part ii, using a line representation, are treated at the MM level.

"distributed approximating functional" propagator.[7,166,167,171,172] Hence, all quantum effects pertaining to the quantized H/D nucleus (zero point, tunneling, as well as overbarrier reflections) as well as those arising from the electronic degrees of freedom within the model were included. The kinetic isotope effect in ref 7 was computed by considering a constrained ensemble average of the ratio of transmission coefficients for hydrogen and deuterium. The constraint limits the ensemble average to the portion of the phase space that is sampled during the reactive process. The transmission coefficients for each case were computed from explicit quantum wavepacket dynamics of the transferring nucleus on potential surfaces obtained from the active site geometry dependent electronic structure as highlighted above. Thus, the electronic and quantum nuclear components are both active site geometry driven, dynamical quantities. These are particularly distinguishing features when considering other methods such as those discussed in refs 41, 42, 161, and 170. While the treatment in refs 41 and 170 involves a vibronically nonadiabatic treatment of a single electron and a single proton that undergo proton-coupled electron transfer as governed by an empirical valence bond (EVB)[22,173−175] surface, the approach in refs 42 and 161 argues a hydrogen transfer mechanism by conducting simulations that employ Feynman path integral approaches[176−178] to describe the trajectory of the quantized hydrogen nucleus, which moves on an enzyme potential surface computed from EVB. By contrast, our approach in ref 7 and the approach discussed in this paper involves the simultaneous dynamical treatment of the full electronic density matrix (that is, all electrons chosen inside an active QM region) in parallel with the nuclear degrees of freedom. Thus, the approaches here and in ref 7 are not restricted to a specific mode of transfer such as proton coupled electron transfer,[41,170] proton transfer, hydrogen transfer, or hydride transfer. However, it must be noted that the main goal of ref 7 was to evaluate coupled quantum-nuclear/electronic contributions to the hydrogen transfer step of the catalytic process. Hence, the exact nature of large-scale rearrangements of the protein that may facilitate gating modes and the contribution of nuclear quantum effects to catalysis were not explicitly probed. Therefore, only reduced active site models were considered. Similar models have been used in previous studies on metalloenzymes.[40,179]

In ref 9, we inspected the hydrogen transfer problem in SLO-1 using the concept of measurement driven quantum evolution. The enzyme active site was treated as a measurement device. The effect it had on the hydrogen transfer process was represented using the potential energy surfaces computed in ref 7. Thus, while the enzyme active site was not included in an atomistic fashion, its effect is accounted for as stated above. We used this analysis to probe whether the action of the enzyme active site during the hydrogen transfer step of the catalysis process could be described using a measurement paradigm. We found these ideas to have utility in providing a qualitative description of the hydrogen transfer step. Several of the qualitative features found in the wavepacket dynamics studies in ref 7, such as the shift in the "transition state" toward the reactant as a result of nuclear quantization, greater participation of excited states in the case of deuterium, and presence of critical points along the reaction coordinate that facilitate hydrogen and deuterium transfer and coincide with nuclear wavepacket surface crossings, were also recovered using the measurement perspective. However, the transfer probabilities obtained from measurement alone were not suficient for a full quantitative description. This suggested that the hydrogen transfer process in SLO-1 may be interpreted as a combination of measurement driven (or active-site driven) evolution and unitary evolution. Similar effects have been noted in the field of coherent control.[180,181] In addition, we also probed the control[9,182−190] of such a transfer process. The idea of control used in ref 9 differed from that in site specific mutagenesis, in that the control of the hydrogen transfer process in ref 9 was facilitated by altering the dynamics of transfer as opposed to structure.
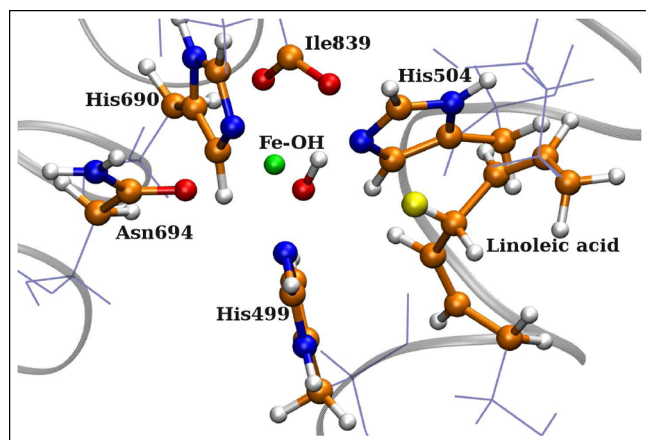
Here, we have studied both model systems similar to those encountered in refs 7 and 9 as well as much larger computational models of the enzyme to elucidate the effect of the active site on the hydrogen transfer process. The methodology used in the current work is the biased ensemble sampling approach described in section II.

A. Description of the Simulated Systems. The initial structure for SLO-1 was obtained from the Brookhaven Protein Data Bank (PDB) entry 1YGE.[191] Next, Autodock4[192] was used to place linoleic acid into the binding pocket through docking calculations. The intrinsic Autodock protocol estimates free energies of binding using an Amber force-field-based

scoring function. The SLO-1:LA binding calculations were carried out using the following protocol: First, the LA was placed in the SLO-1 interior such that the transferring hydrogen was close and oriented toward the iron cofactor. Second, a docking grid of $30 \times 30 \times 15$ Å was generated about the center-of-mass of LA. Finally, during the docking calculation, all hydrogens in LA were explicitly included and the protein was held rigid. 256 different structures were generated. These were filtered on the basis of geometry, and the acceptance criterion was a donor−acceptance distance of ≤ 4 Å. The final structure was chosen on the basis of the orientation of the donor, acceptor, and transferring hydrogen. Using the refined docked structure, we considered the following two QM/MM optimized active site model systems for the AIMD rare events simulations:
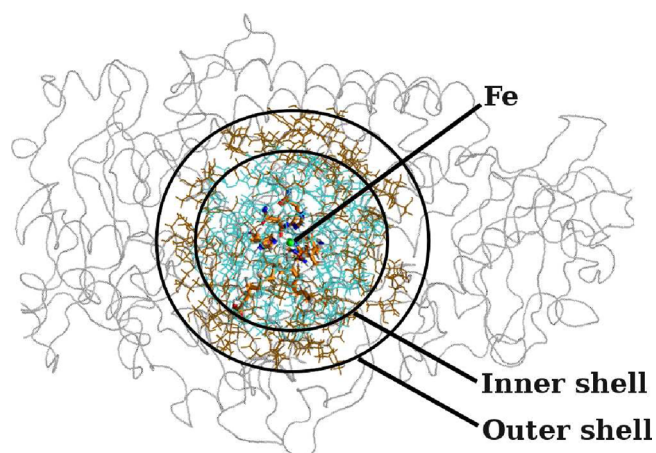
(a) Model-1 contained 50 atoms (Figure 2i). A similar model was employed in the quantum dynamics studies of refs 7 and 9. In refs 7 and 9, such models allowed us to investigate the computationally challenging quantum dynamical properties[7] of the transferring proton along with concerted changes in electronic structure. As a comparative study, we have retained this system here as Model-1.

(b) One goal for this publication is to probe the effect of the dynamics in the active site region on the hydrogen transfer process. In other words, the structural fluctuations of the moieties in close proximity to the active site are to be probed, while the rest of the enzyme's effect on the hydrogen transfer process is restricted. Toward this, as part of Model-2, we apply *asymptotic boundary conditions* on the system as described in Figure 4 with benchmark studies provided here as Supporting

Figure 4. A pictorial representation of the asymptotic boundary conditions enforced in Model-2. The inner shell contains all atoms within a distance of 14 Å from the active site iron center and is represented in cyan. This region is the most flexible part of the enzyme during Model-2 simulations. Atoms that are situated between 14 and 16 Å from the iron center (represented in ochre) are constrained (see text) so as to allow the outer portion (greater than 16 Å from the iron center and represented in gray) to remain frozen during dynamics.

Figure 3. QM region for Model-2 depicting the important Fe-ligands, His499, His504, His690, Asn694, and the Ile839 carboxylate group. The atoms in the QM region are represented in ball-stick representation, and the remaining groups are represented with lines (iceblue) and ribbons (gray). For clarity, the transferring proton is presented in yellow. The color code for the other atoms is as follows: carbon, orange; oxygen, red; nitrogen, blue; iron, green; hydrogen, white.

Information. Specifically, all atoms outside a 16 Å radius from the active site iron-cofactor are frozen during dynamics. Consequently, the atoms inside a spherical shell defined to be between a 14 and 16 Å radius from the iron cofactor are constrained, while the atoms closer to the active site iron are maintained free (that is constraint free) during dynamics. There are 2174 atoms inside the 16 Å shell, and this subsystem is shown in Figure 2ii (a zoomed in version of only the QM

region for Model-2 is shown in Figure 3). In the Supporting Information, we benchmark the numerical constraints to be enforced on the 14−16 Å radius shell such that the dynamics of the region inside 14 Å remains consistent with or without constraints on the 14−16 Å radius shell region. This is especially critical, since we wish to sample that region of the classical phase space that maintains the atoms outside 16 Å at the original configuration. Thus, the dynamics of the region inside 14 Å must be unperturbed by application of constraints. The parameters found to be appropriate in the Supporting Information are the ones used in all the *ab initio* molecular dynamics simulations discussed here.

It must also be noted that there have been studies[24,162,193,194] that have gauged the effect of dynamics far from the active site (beyond 15 Å). These effects are not probed in the current publication. On the contrary, effects orthogonal to the large distant allosteric effects, i.e., those effects that are entirely due to the active site groups within the 14 Å shell region, are probed here while maintaining the surrounding effects to be constant. To this effect, the benchmarks in the Supporting Information are conducted using the hybrid quantum mechanics (b3lyp/lanl2dz)/molecular mechanics (CHARMM[195]) atom-centered density matrix propagation (ADMP)[6,61,108−111] approach discussed in section II, as implemented within a developmental Gaussian version.[139] The hybrid DFT/CHARMM energies and gradients, as dictated by ONIOM, are computed through an interface script that is available upon request from the corresponding author.

The QM system for Model-1 contains 34 atoms including the Fe−OH complex, three histidine residues each modeled as ammonia, the carboxylate group of the terminal Ile839 residue, the carboxamide group of Asn694, and a part of linoleic acid substrate that includes the donor carbon (C_{11}) group sandwiched between a π-bond on either side. The QM system for Model-2 consists of 71 atoms comprising the Fe−OH complex; side chains of His499, His504, His690, and Asn694, the carboxylate group of Ile839, and a portion of the linoleic acid that includes the donor carbon (C_{11}) group sandwiched

between a π-bond on either side. For Model-2, the boundary between the quantum and classical subsystems was augmented through link atoms located to replace (i) the $C_\alpha-C_\beta$ covalent bond for His499, His504, His690, and Asn694, (ii) the $C_\alpha-C$ covalent bond of Ile839, and (iii) the C_7-C_8 and $C_{14}-C_{15}$ bonds for linoleic acid.

For the ADMP rare-events sampling dynamics calculations, a fictitious inertia-tensor scale value of 0.1 amu·bohr^2 ($\approx$180 a.u.)[108] is found along with a time-step of 0.25 fs for Model-1 and 0.1 fs for Model-2. These values are consistent with previous studies.[6,108]

B. Results from ADMP Simulations of Rare Events in Model-1 and Model-2.

In addition to extensive studies focused on kinetic and isotope properties,[24,37,39−42,159,165,196,197] site-specific mutagenesis studies have also been carried out on SLO-1. These studies have been directed toward probing the influence of a number of hydrophobic residues that are in close proximity to the enzyme active site and include Ile553, Leu546, and Leu754. It is learned that the side chains of Leu546 and Leu754 are critical toward maintaining a favorable orientation of linoleic acid relative to the active site Fe−OH complex.[37,198] Another bulky distant residue, Ile553, that is located ∼15 Å from the active site iron-cofactor has been indicated to be crucial for modulating the donor−acceptor distance fluctuations.[193,194]

Most of the above-mentioned research has been directed toward investigating the change in donor−acceptor distance, or hydrogen transfer gating properties, either through alterations to electrostatic properties of donor/acceptor groups or due to change in steric properties (bulkiness) of surrounding amino acid residues that are close to donor/acceptor atoms. Here, we probe alterations to electrostatic properties of the acceptor and donor groups through structural constraints on the surrounding active site atoms. The effect of structural flexibility of the active site groups on the proton transfer process is probed through simulations employing the rare-events sampling approach for classical AIMD discussed in section II. Specifically, three sets of parameters are analyzed to gauge such flexibility:

(a) The hydrogen bonding nature of the active site and its effects on the hydrogen transfer process are evaluated. Toward this, we modify the hydrogen bonding properties of the acceptor oxygen through structural constraints (see η in eq 1 and $\mathbf{K}$ in eq 2) on the Ile839 protein backbone carboxylate group due to its hydrogen bonding propensity (see Figure 3). Similar constraints on the structural fluctuations in the active site can be enforced through amino acid mutations that affect the noted hydrogen bonding property. In addition, more subtle effects can be obtained by introducing isotope substitutions for the atoms participating in hydrogen bonds, and the computational treatment of heavier isotope substitution will be the subject of future publications.

(b) The effect of active site structural freedom on the hydrogen transfer process is evaluated through structural constraints on all active site groups. These constraints allow us to explore the role of the dynamical fluctuations of individual groups on the electrostatic properties of donor/acceptor atoms.

(c) Electronic effects as they arise from the flexibility studies in (a) and (b) are also probed in this study.

The constraint parameters used to describe bath variables are outlined in Table 1. The choice of these parameters is dictated by the following considerations: The donor (carbon), the acceptor (oxygen), and the transferring hydrogen are to be tethered to bath particles that drive the transfer process which

Table 1. Summary of Constraints for All Simulations

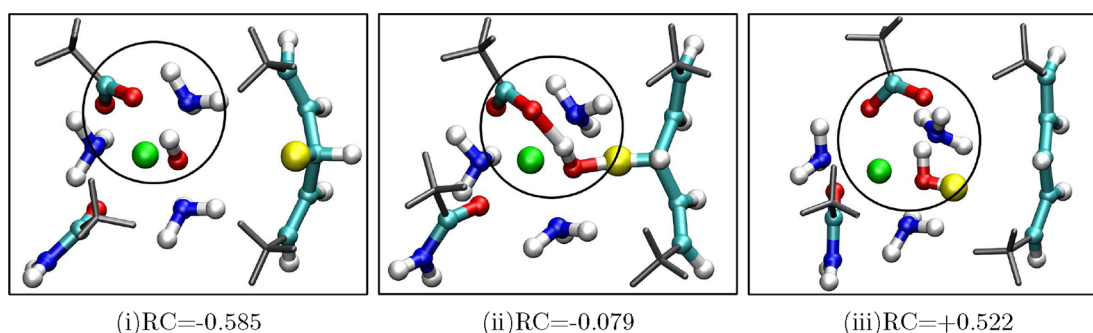| Model-1		
simulation set	constrained groups	force constant $\mathbf{K}$ (eq 2)[a]
Set-1	donor[b]	15570 pN/Å[c] 469 cm^{-1}
	acceptor[a]	15570 pN/Å 406 cm^{-1}
	hydrogen[a]	15570 pN/Å 1624 cm^{-1}
Set-2	donor[a]	15570 pN/Å 469 cm^{-1}
	acceptor[a]	15570 pN/Å 406 cm^{-1}
	hydrogen[a]	15570 pN/Å 1624 cm^{-1}
	carboxylate group (COO$^-$)[d]	15570 pN/Å 469 cm^{-1} [e]
Model-2		
simulation set	constrained groups	force constant $\mathbf{K}$ (eq 2)
Set-1	donor[a]	15570 pN/Å 469 cm^{-1}
	acceptor[a]	15570 pN/Å 406 cm^{-1}
	hydrogen[a]	15570 pN/Å 1624 cm^{-1}
Set-2	donor[a]	15570 pN/Å 469 cm^{-1}
	acceptor[a]	15570 pN/Å 406 cm^{-1}
	hydrogen[a]	15570 pN/Å 1624 cm^{-1}
	Ile839 (COO$^-$)[b]	15570 pN/Å 469 cm^{-1} [c]
Set-3	donor[a]	15570 pN/Å 469 cm^{-1}
	acceptor[a]	15570 pN/Å 406 cm^{-1}
	hydrogen[a]	15570 pN/Å 1624 cm^{-1}
	His499, His504, His690, Asn694, Ile839 (COO$^-$)[b]	155690 pN/Å[f] 1483 cm^{-1} [c]

[a]The force constant is provided in units of pN/Å and cm^{-1}. The latter is obtained by utilizing the mass of the atom on which the constraint is applied. [b]The donor, the acceptor, and transferring hydrogen are coupled to bath variables, that bias the dynamics of these quantities toward achieving the transfer process. The force constants mentioned in these cases are related to η (eq 1) and $\mathbf{K}$ (eq 2). [c]The quantity 15570 pN/Å ≈ 224.10 kcal/mol·Å^2. [d]These groups are harmonically constrained to remain close to their original positions. The harmonic force constants are as noted. The goal is to probe the effect of the dynamics of these groups on the transfer process. [e]Computed assuming carbon mass. [f]The quantity 155690 pN/Å ≈ 2240.82 kcal/mol·Å^2. The stringent constraint probes the effect of active site flexibility. See text here and also in section IIIC.

is designated to be a rare event. This is on account of the 11 kcal/mol[7] activation barrier. Consequently, the masses for these bath degrees of freedom are chosen to be large so as to achieve the transfer process. This description is along the lines of a large mass object steering a smaller mass over a barrier. However, it is also necessary to allow configurational sampling during the biased transfer process. As a result, the force constants on the individual donor, acceptor, and transferring hydrogen, as dictated by the choice of $\mathbf{K}$ in eq 2 (also see η in eq 1), are to be reasonably small. Consequently, we wish to attach the three particles to heavier surrogate degrees of freedom with weaker springs coupling the individual bath particles to the real particles. (Note that a force constant that is too small essentially deems the rare event computationally intractable to achieve, whereas a value too large yields limited configurational sampling during the transfer process. Hence, a compromise between efficiency of transfer and configurational sampling is essential in the choice of force constant.) The donor (carbon), acceptor (oxygen), and the transferring proton were tethered to bath particles (see $\tilde{R}$ in eqs 1 and 2) where the constraint η is chosen to be harmonic with a force constant of 15570 pN/Å. The units for force constants used here are commensurate with those in the rare events sampling literature[51,27] and in the
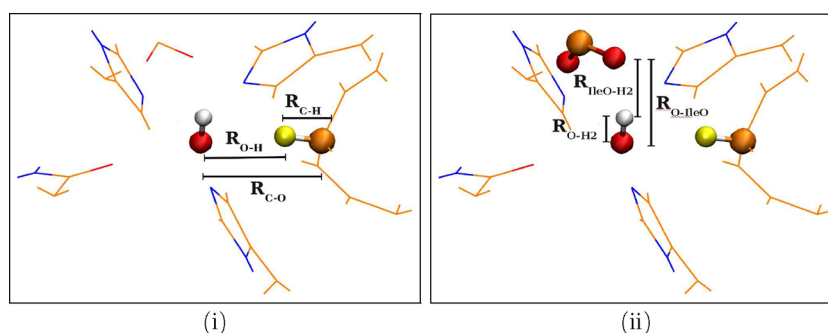
Figure 5. (i) Reaction coordinate (eq 28) defined using the donor carbon (represented in orange), acceptor oxygen (red), and hydrogen (yellow). (ii) Hydrogen bond coordinate (RC$_{Hbond}$: eq 29) defined between Ile839 oxygen (red), acceptor oxygen (red), and hydrogen bonded to the acceptor oxygen (white).

Figure 6. Typical snapshots from the productive Model-1, Set-1 (unconstrained Ile839) simulations depicting the hydrogen transfer between linoleic acid and the acceptor OH: (i) reactant state; (ii) shared proton state; (iii) product state. Part ii indicates a stable hydrogen bond network that appears to facilitate the transfer process. As noted, when the hydrogen bond formation between Ile839 and the acceptor group is hindered, the hydrogen transfer process is also adversely affected, as seen in Figure 7.

atomic force microscopy literature.[199] In units more commonly used in chemistry, 15570 pN/Å ∼224.10 kcal/mol·Å². This harmonic force constant corresponds to a frequency ($\bar{\nu}$) of about 469 cm^{-1} on the carbon atom where the constraints are applied. The frequency is estimated using $k = 4\pi^2 c^2 m\bar{\nu}^2$, where c is the velocity of light, m is the mass of the particle in question, and $\bar{\nu}$ is the frequency in cm^{-1}. The corresponding frequency for the other donor/acceptor or transferring hydrogen atoms are in Table 1. Consistent with the requirement of heavier bath particles, the masses for the bath particles tethered to the donor and acceptor are 500 amu, whereas the degrees of freedom tethered to the transferring hydrogen have a mass of 100 amu. It may be noted from Table 3 and Figure 12 (which is discussed in Appendix A) that the magnitude of the mass chosen for these bath degrees of freedom is inversely proportional to the transfer rate, allowing larger sampling of the remaining degrees of freedom during the transfer process. The simulations were carried out starting at a temperature of 300 K. The initial kinetic energy for all bath particles was chosen to be 12 kcal/mol. This provides sufficient momentum to the system to overcome the activation barrier. The initial velocities of the bath particles tethered to the donor carbon and transferring hydrogen were directed toward the initial position of the acceptor oxygen atom. Similarly, the initial velocity of the fictitious particle tethered to the acceptor oxygen was directed toward the initial position of the donor carbon atom. That is, the directions of the initial velocities of the fictitious particles were chosen to assist the hydrogen transfer process. Under these conditions, a large variety of simulations were performed, that amount to multiple equilibrated temperatures (or nuclear kinetic energies) inside a narrow window. These simulations are summarized in

Appendix B and in the remaining section of this paper; the general qualitative trends consistent with this larger body of simulations are highlighted below.

We monitor the hydrogen transfer event through evolution of the reaction coordinate depicted in Figure 5i and defined as

$$RC = (R_{CH} - R_{OH})/R_{CO} \qquad (28)$$

The quantity RC above is a function of the simulation time where atoms C, O, and H refer to the donor carbon (C$_{11}$), acceptor oxygen (O), and transferring hydrogen (H), respectively. However, also note that the simulation time used here is a quantity that measures the effectiveness of the *assisted* hydrogen transfer process. In this study, we have not considered a normalization of this time variable to explicate its correspondence to the real time variable. The primary goal of the current publication is to evaluate the rare events sampling methodology presented in section II, and a secondary goal is to estimate the extent to which dynamical fluctuations within the active site affect the transfer process. Thus, connections between the time variable introduced here through biased dynamics and the real time variable will be considered in future publications.

In addition to the above-mentioned simulations (denoted as Set-1, see Table 1), additional simulations were carried out in which the carboxylate group of Ile839 is harmonically constrained with a force constant of 15570 pN/Å (∼224.10 kcal/mol·Å²) to investigate the role of the Ile839 carboxylate group on the transfer reaction. These simulations are denoted as Set-2 in the discussion below. The carboxylate oxygen in Ile839 appears to be close enough to be hydrogen bonded to the acceptor oxygen (see Figure 5ii). As a result, one aspect that

is probed through these simulations is the indirect effect on the hydrogen transfer process resulting from a control placed on the Ile839−acceptor hydrogen bond (RC$_{Hbond}$; see Figure 5ii), defined as

$$RC_{Hbond} = (R_{O-H2} - R_{IleO-H2})/R_{O-IleO} \qquad (29)$$

The quantity RC$_{Hbond}$ is a function of the acceptor oxygen (O), the hydrogen atom (H2) bonded to the acceptor oxygen, and the Ile839 oxygen (IleO) atoms over the course of the simulation. We first present results from the Model-1 simulations. We then support these results using the more realistic Model-2 simulations. In all cases, a more exhaustive set of simulations that support the trends presented here can be found in Appendix B.

1. Influence of the Secondary Hydrogen Bond between the Acceptor OH and the Ile839 Carboxylate Oxygen on the Hydrogen Transfer Process in Model-1. In this section, we illustrate the effect of the hydrogen bond between Ile839 and the acceptor group on the hydrogen transfer between donor and acceptor groups.

For the unconstrained simulation (Set-1), the key hydrogen transfer steps are displayed in Figure 6 and the typical variations in RC (Figure 5i) and RC$_{Hbond}$ (Figure 5ii) as a function of the biased simulation time are displayed using black and blue curves, respectively, on the top panel of Figure 7i. (The RC
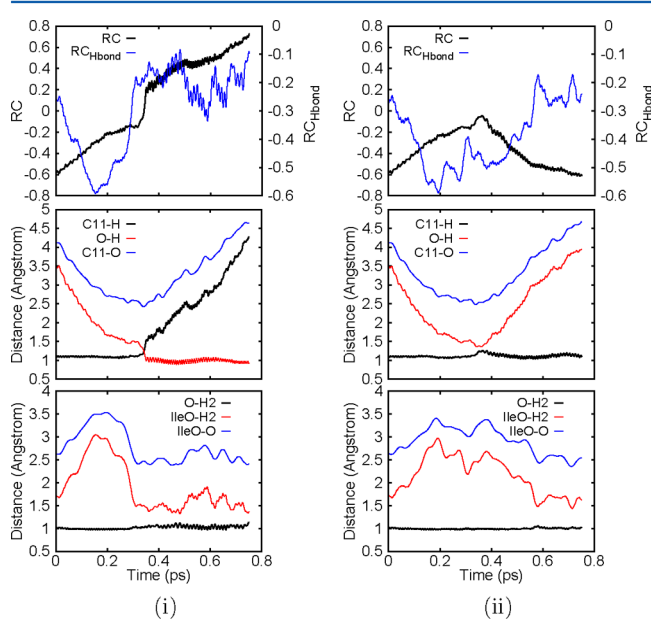
Figure 7. The figure displays results for Model-1: (i) unconstrained simulation (Set-1); (ii) Ile839 constrained (Set-2). In each subfigure, the top panel displays RC (eq 28) in black and RC$_{Hbond}$ (eq 29) in blue. The center panel displays distance evolution between donor carbon (C$_{11}$), hydrogen (H), and acceptor oxygen (O) atoms. The bottom panel displays the distance evolution between Ile839 oxygen (IleO), hydrogen bonded to acceptor O (H2) and acceptor oxygen (O) atoms.

data for an exhaustive set of simulations is provided in Figure 13iii and iv, as part of Appendix B.) For all the productive Set-1 simulations shown in Table 4, during the initial ∼350 fs of the biased simulation, the distance between the donor carbon (C$_{11}$) and the acceptor oxygen (denoted as O) decreases (for example, the blue curve in center panel of Figure 7i) due to displacement of the acceptor OH toward linoleic acid. As a result, the acceptor OH

moves away from Ile839. (The distance between the Ile839 oxygen atom and the acceptor oxygen is denoted in the discussion below as IleO−O.) This increases IleO−O during the initial ∼200 fs of simulation (the blue curve in the bottom panel of Figure 7i) and weakens the hydrogen bond between Ile839 and the acceptor OH. (the blue curve in the top panel of Figure 7i). The unconstrained Ile839 carboxylate group then moves toward the acceptor oxygen, forming a hydrogen bond (typical behavior shown in Figure 6ii), as indicated by a sharp increase in RC$_{Hbond}$. These structural transformations lead to a continued increase in electronegativity of the acceptor oxygen, to facilitate the hydrogen transfer. In this respect, compare the Mulliken charge on the acceptor oxygen between simulation sets 1 and 2 (Figure 8). It may be noted that the acceptor
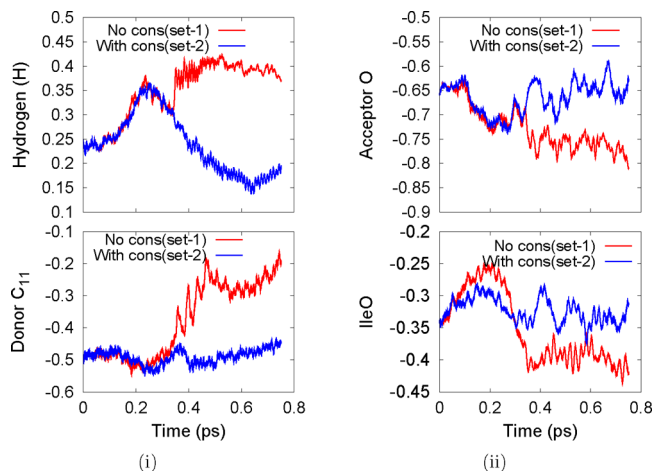

Figure 8. Evolution of the Mulliken charge of active site atoms for Set-1 (red) and Set-2 (blue) simulations for Model-1: (i) top panel: transferring hydrogen (H), bottom panel: donor carbon (C$_{11}$); (ii) top panel: acceptor oxygen (O), bottom panel: Ile839-oxygen (IleO).

oxygen becomes more electronegative in the unconstrained Set-1 simulation following the formation of the IleO−O hydrogen bond. In addition, these processes are concomitant to the decrease in the distance between the acceptor O and the transferring hydrogen (denoted as "O−H" in Figure 7i), leading to the hydrogen transfer. This is also indicated by the increase in the C$_{11}$−H distance (black curve in the center panel of Figure 7i) and decrease in the O and H distance (red curve in center panel of Figure 7i). Note the crossing of the black and red curves in the center panel of Figure 7i which is an indication of the proton transfer. Such a crossover is absent in Set-2 (Figure 7ii), which indicates that there is no hydrogen transfer in Set-2. Following the proton transfer, the donor atom C$_{11}$ loses negative charge that is spread over the neighboring carbon atoms C$_{10}$ and C$_{12}$ of linoleic acid. This aspect is, of course, to be expected on the basis of the delocalization of the free radical on C$_{11}$ on account of the neighboring π-bonds.

It is also interesting to note the charge on the transferring hydrogen nucleus, as seen in Figure 8. Following the transfer process, the charge on the transferring hydrogen becomes more electropositive in the unconstrained simulation. This is coordinated with an increase in positive charge on the donor C$_{11}$ and increase in negative charge on the acceptor.

These simulations for Model-1 thus indicate that establishment of the hydrogen bond between Ile839 and the acceptor group facilitates the hydrogen transfer. The results here are
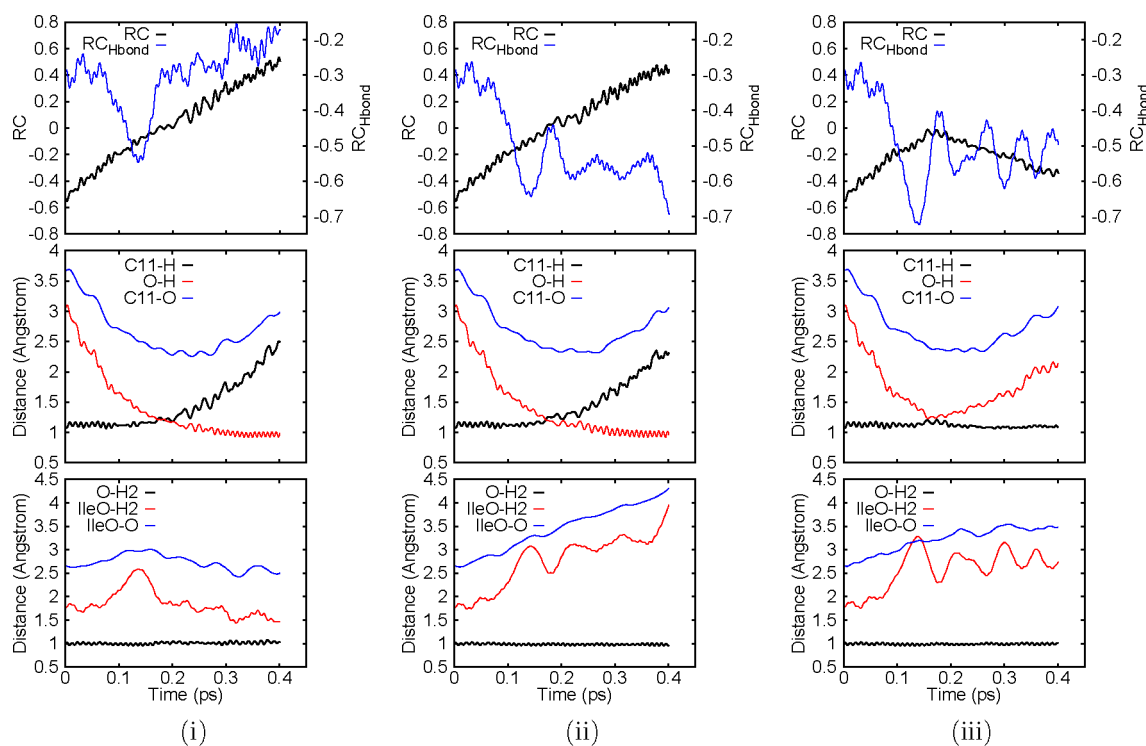
Figure 9. For Model-2, the time evolution of the reaction coordinate for (i) unconstrained Ile839 (Set-1), (ii) constrained Ile839 (Set-2), and (iii) a simulation in which all active site residues except the donor (linoleic acid) and acceptor (Fe−OH complex) groups were constrained (Set-3). See Table 1 for simulation details. In each subfigure, the top panel displays RC (eq 28) in black curve and RC_{Hbond} (eq 29) in blue. The center panel depicts positions of the donor carbon (C_{11}), hydrogen (H), and acceptor oxygen (O) atoms relative to each other. The bottom panel displays the distance evolution between Ile839 oxygen (IleO), hydrogen bonded to acceptor O (H2) and acceptor oxygen (O) atoms.

further substantiated through an extended set of simulations constructed at multiple temperatures and discussed in Appendix B. Note the similarity between the black curve in the top panel of Figure 7 and the reddish, higher temperature, curves in Figure 13iii and iv. Note that, while a large fraction of the simulations in Set-1 yield a transfer (except the few low temperature processes depicted in Figure 13iii), a much higher temperature is required in Set-2 to achieve a hydrogen transfer. This higher temperature is necessitated by the constraint on Ile839. See the discussion in Appendix B.

2. Active Site Flexibility Is Crucial for Hydrogen Transfer in Model-2. In Model-2, the time evolution of RC for unconstrained Ile839 exhibits qualitatively similar behavior as that in Set-1, Model-1. (A typical behavior for Model-2, Set-1 is shown in Figure 9i, with a more exhaustive study depicted in Figure 14iv. Compare Figure 9i or Figure 14iv with Figure 7i to note the qualitatively similar RC evolution between Model-1, Set-1 and Model-2, Set-1.) A typical Model-2, Set-1 simulation begins with a decrease in the donor (C_{11})−acceptor O distance (the blue curve in the center panel of Figure 9i) followed by sequential hydrogen transfer from C_{11} to O (see Figure 10i−iv: follow the transferring hydrogen in yellow). One critical observation is the concomitant change in the orientation of the Ile839 carboxylate group along with movement of the acceptor group so as to maintain the hydrogen bond during the hydrogen transfer process (Figure 10iii and iv). Furthermore, the productive Set-1 simulations presented here and in Appendix B have donor−acceptor distances in the range 2.67 ± 0.4 through 2.71 ± 0.4 Å.

To gauge the effect of constraining Ile839 for Model-2, we carried out simulations where the Ile839 carboxylate group was

harmonically constrained as in Model-1, Set-2 with a force constant of ~15570 pN/Å (~224.10 kcal/mol·Å²), as noted in Table 1. The proton transfer occurs despite the constraints on Ile839, as seen from the top panel in Figure 9ii and from Figure 14v. This is related to the fact that the overall flexibility of the active site is maintained to a large extent in Set-2. In Section IIIC, we introduce a flexibility index parameter derived from a singular value decomposition (SVD)[130,200,201] of the simulation data, which indicates that the active site flexibility is maintained in Set-2 at approximately the same level as in Set-1, despite the constraints on Ile839. Hence, unlike Model-1, the hydrogen bond constraint on Model-2 does not affect the flexibility and hence the transfer process to a large extent. This raises the question as to whether the role of Ile839 in Model-1 is carried out by a collective effort from one or more active site residues in Model-2. To probe this, we carried out additional simulations (named as Set-3) in which all active site residues (side chain atoms of His499, His504, His690, Asn694, and carboxylate group of Ile839), except the donor (linoleic acid) and acceptor (Fe−OH complex) groups, were harmonically constrained with a force constant of ~155690 pN/Å (~2240.82 kcal/mol·Å²) as noted in Table 1. Overlapping snapshots of a typical Set-3 trajectory along with the starting reactant structure are shown in Figure 10 and indeed demonstrate the relatively frozen nature of the active site groups in Set-3. In the figure, the initial reactant structure is represented in transparent gray. During the first half of the trajectory, the donor−acceptor distance gradually decreases such that the transferring hydrogen atom is almost equally shared between C_{11} and the acceptor oxygen atom (Figure 10x and xi). However, due to inhibited structural flexibility, the Ile839 carboxylate group does not form
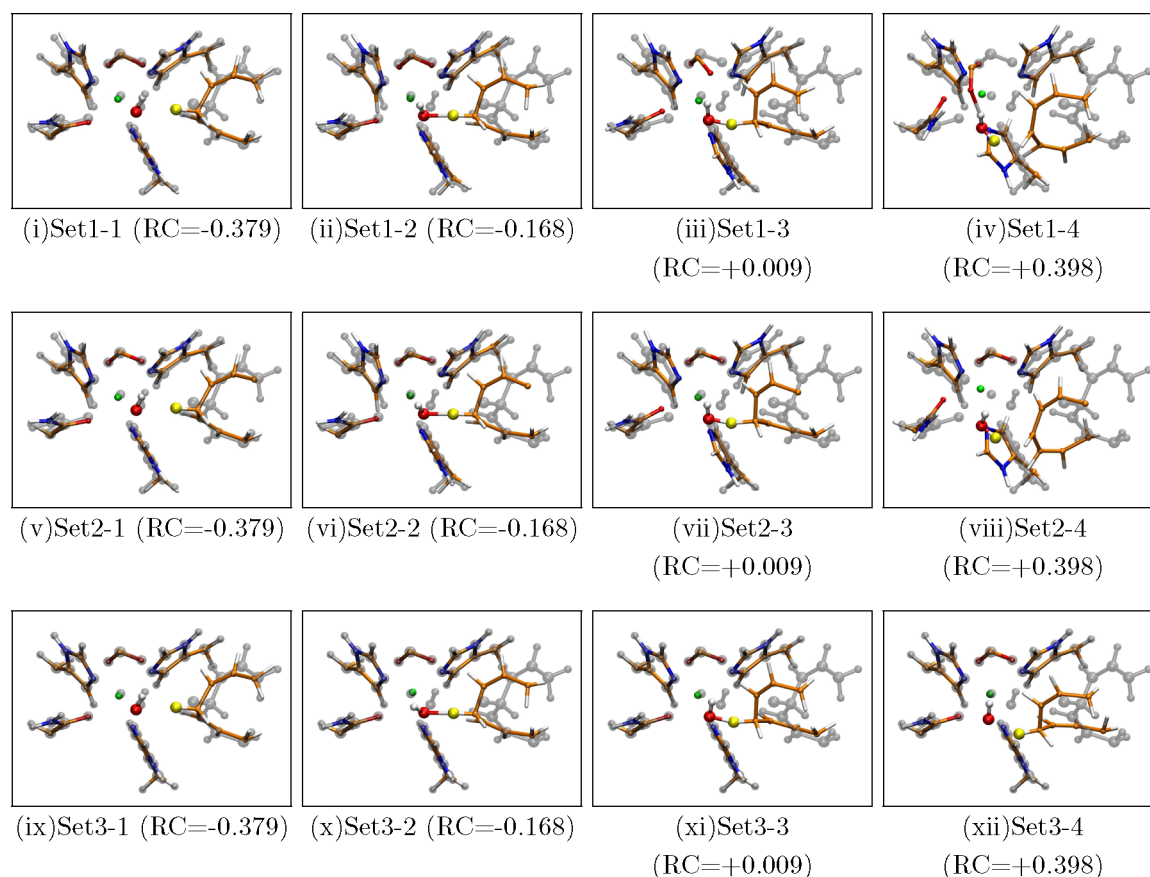
Figure 10. Typical snapshots from the Set-1(i−iv), Set-2(v−viii), and Set-3(ix−xii) simulations for Model-2. In each panel, the transparent system represents the starting (reactant) structure and the opaque representation shows the active site structure at a later step along the dynamics trajectory. The opaque figures are arranged in increasing order of time. That is, panels i, v, and ix represent the early portion of the dynamics. Panels ii, iii, vi, vii, x, and xi represent structures in which transferring hydrogen (shown as yellow sphere) is shared between the donor and acceptor groups. Finally, panels iv and viii represent a structure in which the hydrogen atom is transferred onto the acceptor group and panel xii shows the proton localized on the donor group due to the constrained active site geometry.

a hydrogen bond with the acceptor (Figure 10xi). This is in contrast to that observed in Set-1 of Model-2 (Figure 10iii) and in Set-1 of Model-1 (Figure 6ii). Subsequently, the proton remains localized on the donor group and the transfer does not occur in Set-3 (Figure 10xii). The results here are substantiated through additional simulations with different initial conditions, to ensure better statistics, and these are discussed in Appendix B.

To further understand the role of Ile839 in the proton transfer process for Model-2, we monitored RC_{Hbond} (defined in eq 29) for all three sets of Model-2 simulations mentioned above. With no harmonic constraints on Ile839, Set-1 exhibits a qualitatively similar trend as that for Model-1 (compare top panels of Figures 7i and 9ii). Note that, in Model-1, the bell-shaped feature that exhibits sequential increase in RC_{Hbond} followed by decrease in the distance between Ile839 and the acceptor oxygen happens more gradually for Model-2 (the blue curves in the bottom panel of Figures 7i and 9i). On the other hand, as compared to Model-1, Set-2 and Set-3 simulations in Model-2 exhibit significant differences. As a result of constraints, the Ile839 carboxylate motion is significantly reduced in both Set-2 and Set-3. The acceptor group shows higher structural motion in Set-2 as compared to Set-3 where the entire active site is constrained.

Behavior of the Mulliken charge evolution for Model-2 is presented in Figure 11. We note that Set-1 and Set-2 display
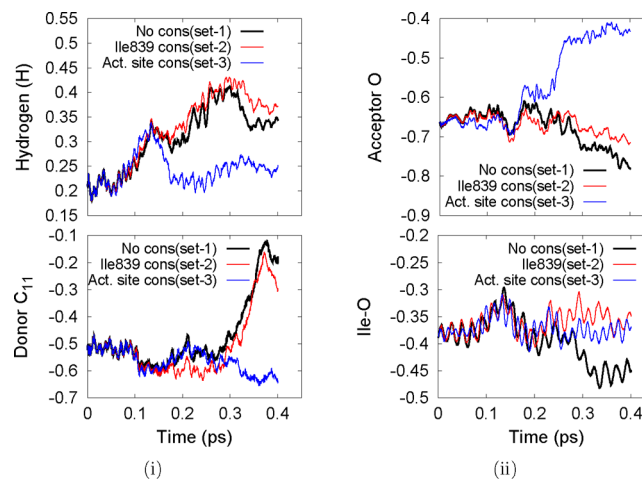
Figure 11. Evolution of Mulliken charges for the active site atoms in the Model-2 simulations with Set-1 shown in red, Set-2 in green, and Set-3 in blue.

similar charge evolution trends; however, the charge evolution for Set-3 is similar to that seen in Set-2 of Model-1. As seen earlier, the charges for Set-1 indicate that during the hydrogen transfer the donor C_{11} becomes more electropositive by about 0.2−0.3 units. This aspect is generally consistent in both

Model-1 and Model-2. Compare the red curves in Figures 8 and 11. This is not the case for the controlled Set-3, Model-2 and Set-2, Model-1 calculations which affect the transfer process. The growth in the C_{11} charge by approximately 0.2−0.3 units seems to suggest that the donor species, post hydrogen transfer, is a delocalized radical, where the delocalization is facilitated by the neighboring double bonds between C_9−C_{10} and C_{12}−C_{13}. *The magnitude of growth in the C_{11} charge appears to suggest that the process is a hydrogen-atom transfer process. However, it is also clear from the evolution of charge on the acceptor oxygen and the transferring hydrogen that the transferred electron and proton do not appear on the acceptor side in one piece.* A more detailed examination of the charge evolution will be considered as part of a future publication.

To summarize, the SLO-1 hydrogen transfer simulations presented here were carried out with multiple system sizes: Model-1 contained 50 atoms, while Model-2 had 2174 dynamic atoms; the dynamical subset of atoms in Model-2 were obtained by enforcing asymptotic boundary conditions on the full enzyme. Model-1 has a simplified and reduced active site, while Model-2 contains the enzyme. While the intricate details of the hydrogen bond formation and structural changes differ between Model-1 and Model-2, an important feature that is apparent from these simulations is that the proton transfer occurs in sets where the hydrogen bond formation takes place either through flexibility of Ile839 or through a *concerted* action involving an ensemble of active site groups. The statistical significance of the results presented here is discussed in Appendix B.

The analysis presented above thus emphasizes the importance of structural flexibility of the protein residues surrounding the donor−acceptor groups on the rate-limiting hydrogen abstraction step. This flexibility is quantitatively probed in the next section through the introduction of an active site flexibility parameter computed from the dynamics trajectory data.

C. Quantitative Evaluation of the Flexibility of the Active Site from the Dynamics Simulations. We have noted in the previous sections that the flexibility of the enzyme active site is critical toward facilitating the hydrogen transfer process. Structural constraints restrict the dynamics to remain in specific regions of the phase space to limit the reactive process. As noted earlier, these constraints can be enforced using an ensemble of amino acid mutations. In this section, we introduce a measure of active site flexibility. This measure allows us to gauge the extent to which the active site dynamics is quantitatively perturbed while affecting the hydrogen transfer process.

In essence, we are interested in gauging the rigidity introduced in the active site as a result of these constraints. Over the years, significant research has been directed toward studying mechanical properties of biological systems. Examples include techniques such as atomic force microscopy (AFM)[199] and optical tweezers.[202] For example, Kinney et al. have measured elastic properties such as Young's moduli of human dentine to show that tubule orientation had no appreciable effect on the mechanical properties of normal dentine.[203] AFM experiments on protein mechanics have indicated how unfolding and refolding of specific protein domains may be responsible for carrying out mechanical functions such as maintaining protein tension.[204] Critical protein−protein interactions[205] are controlled through AFM to probe the extent to which these are responsible for maintaining structural stability of cells and tissues. Mechanical properties of biological surfaces such as those in human platelets have also been studied.[206]

Investigations of nanomechanical properties of biomolecular systems such as DNA, RNA, microtubules, and actin filaments have been used to elucidate molecular capability in imparting twist motions.[202] Optical tweezer studies have also significantly enhanced our understanding of nanomechanical properties of biopolymers such as nucleic acids and polypeptides.[207,208] Here, as stated above, we probe the effect of mechanical restrictions on an enzyme reactive process. Such studies are only possible here, on account of the *ab initio* nature of the potential used for the active site.

We first define a fluctuation matrix, $\mathbf{X}$, with elements given by $\mathbf{X}_{i,j} \equiv \mathbf{R}_i(t_j) - \mathbf{R}_i(t_0) = d_i(t_j)$, where the index i takes on values between 1 and $3N$ and the index j represents the time sample obtained from the trajectory. Thus, $\mathbf{X}$ is a $3N \times T$ matrix, with T being the number of simulation samples, and describes the fluctuations in the position vectors of the N atoms that are chosen to be those from the active site, comprising His499, His504, His690, Asn694, Ile839, FE−OH complex, and linoleic acid. We then carry out a singular value decomposition (SVD)[130,200] of the fluctuation trajectory matrix, $\mathbf{X}$:

$$\mathbf{X} = \mathbf{U}\mathbf{\Sigma}\mathbf{V}^\mathbf{T} \tag{30}$$

where $\mathbf{U}$ and $\mathbf{V}^\mathbf{T}$ are orthogonal matrices and $\mathbf{\Sigma}$ is a diagonal singular value matrix. Since the rows of $\mathbf{X}$ signify a time-evolution of all the $3N$ coordinates relative to the initial structure, the rows of the quantity $\mathbf{U}^\mathbf{T}\mathbf{X}$ represent the time-evolution of a set of orthogonal coordinates (or principal components of the dynamics) that are determined from the singular value decomposition. Furthermore, $\mathbf{\Sigma}$ represents the extent to which the principal components contribute toward the chosen dynamics trajectory sample. Toward this, Table 2

Table 2. Singular Values and Flexibility Index of the Active Site for the Model-2 Simulations

	Set-1	Set-2	Set-3
Σ_1	718.267	704.753	581.642
Σ_2	184.199	181.311	111.710
Σ_3	77.139	73.089	58.223
Σ_4	62.215	62.117	50.076
Σ_5	41.507	40.803	37.991
volume of hypercube ($\mathcal{V}$)	2.636×10^{10}	2.367×10^{10}	0.7197×10^{10}
flexibility index ($\bar{\mathcal{V}}$)	1.00	0.898	0.273

summarizes the five largest singular values for all Model-2 simulations. The corresponding principal vectors from $\mathbf{U}$ are the ones that have the highest contributions toward the dynamics.

Since the singular values represent the relative contributions of each mode along the left singular, $\mathbf{U}$, vectors toward the total motion of the molecule, the first few modes with highest singular values define an essential subspace (or a hypercube in the phase space) in which the dynamics trajectory prevails. The volume of this hypercube may then be defined as a product of the corresponding singular values

$$\mathcal{V} = \prod_{i=1}^{i=N_{max}} \Sigma_i \tag{31}$$

that can be considered as a measure of the flexibility of the active site. The quantity above may also be interpreted as the maximum spread of a projected phase space distribution function as defined using the positions of the chosen set of

atoms (which in this case is the active site atoms defined above). The quantity N_{max} above is chosen to be 5 in this study. We next define a flexibility index ($\bar{\mathcal{V}}$) as a ratio of the volume of the hypercube for a given simulation, relative to that for Set-1, i.e.,

$$\bar{\mathcal{V}} = \frac{\mathcal{V}^{set-j}}{\mathcal{V}^{set-1}} \tag{32}$$

where, $\mathcal{V}^{set-j}$ is the volume of the hypercube for Set-j. The corresponding values are presented in Table 2.

In Set-1, in absence of constraints, the active site atoms exhibit larger fluctuations accompanied by hydrogen transfer between the donor−acceptor groups. This is indicated by higher Σ values as well as high flexibility index, $\mathcal{V}$ (Table 2). With the harmonically constrained Ile839 in Set-2, the flexibility in the active site is marginally reduced ($\bar{\mathcal{V}} = 0.898$) relative to the fully unconstrained active site in Set-1, and consequently, the hydrogen transfer is *not* inhibited (see section IIIB2). On the other hand, when the active site atoms are stringently constrained (Set-3), the fluctuations and consequently the flexibility are reduced significantly (note, for Set-3, $\mathcal{V}$ is ~27% relative to Set-1) and hydrogen transfer reaction is inhibited. Thus, $\bar{\mathcal{V}}$ provides a quantitative description of the limits placed by the constraints on the dynamical sampling process. In essence, the region of the phase space sampled during Set-2 is approximately 27% of that sampled during Set-1. This reduced sampling has a direct effect on the transfer process.

IV. CONCLUSIONS

In this publication, we introduce a rare events sampling methodology, that includes the simultaneous dynamical treatment of nuclear and electronic degrees of freedom. Starting from

Table 3. Energy Conservation Summary

	$\tilde{M}^a$ (amu)	time (ps)	temp^b (K)	bath particle^c kinetic energy (kcal/mol)	ΔE^d (kcal/mol)
BOMD	700	3.5	234.7	4.6	0.015
	70	1.9	219.2	20.8	0.007
ADMP	700	3.6	224.5	4.6	0.039
	70	1.3	213	20.8	0.015

^{a}The mass of the bath degree of freedom. ^{b}The temperature is calculated from the kinetic energy of the system. ^{c}The initial kinetic energy provided to the bath degrees of freedom. $^d\Delta E$ represents the standard deviation of the total energy of the system during the simulation. This indicates the accuracy of the integration performed on eqs 3−5.
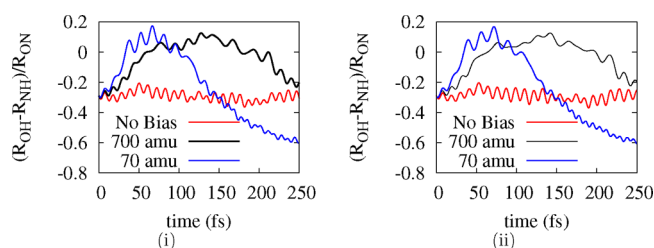
Figure 12. The evolution of the reduced dimensional reaction coordinate, $(R_{OH} - R_{NH})/R_{ON}$ as a function of time. BOMD results are presented in part i, and ADMP is shown in part ii. Clearly, the biased trajectories effectively steer the shared hydrogen over the large potential barrier and toward the acceptor.

Table 4. Summary of Simulations for Model-1: Set-1^a

system nuclear kinetic energy (average ± rms)		system potential energy^b (average ± rms)	hydrogen transfer?
Kelvin^c	kcal/mol	kcal/mol	
175.72 ± 26.05	25.67 ± 3.81	33.31 ± 7.08	no
178.74 ± 28.12	26.11 ± 4.11	33.07 ± 6.82	no
188.74 ± 35.24	27.57 ± 5.15	25.70 ± 9.11	yes
192.08 ± 34.41	28.06 ± 5.03	25.72 ± 8.71	yes
193.19 ± 39.60	28.22 ± 5.78	25.38 ± 9.14	yes
197.82 ± 42.77	28.89 ± 6.25	25.99 ± 8.35	yes
198.56 ± 42.38	29.00 ± 6.19	23.86 ± 7.90	yes
198.83 ± 46.37	29.04 ± 6.77	26.29 ± 9.41	yes
199.24 ± 43.57	29.10 ± 6.36	25.24 ± 8.37	yes
200.93 ± 43.12	29.35 ± 6.30	24.41 ± 7.90	yes

^{a}In all cases, the total energy (defined by the Hamiltonian in eq 17 of the main paper) is conserved to within a 100th of a kcal/mol. A horizontal line in the table below differentiates the productive simulations from the unproductive ones. Clearly, as the average kinetic energy of the system grows, the propensity for a productive simulation also grows. The transition point in this respect appears to be between an "activation kinetic energy" of 26.11 and 27.58 kcal/mol. Note that this is the amount of energy provided to the entire system and not just the reaction coordinate. Also note that the system potential energy is higher (and hence less stable) for the unproductive simulations. This aspect is also noted from Figure 13i. ^{b}Potential energy change during the simulation. Note the larger potential energy change for the unproductive simulations. This is also witnessed in Figure 13i where the unproductive runs show higher potential energy. ^{c}Computed from the nuclear kinetic energy using the equipartition theorem $(3/2(N - 1)kT)$.

Table 5. Summary of Simulations for Model-1: Set-2^a

system nuclear kinetic energy (average ± rms)		system potential energy^b (average ± rms)	hydrogen transfer?
Kelvin^c	kcal/mol	kcal/mol	
235.15 ± 40.47	34.35 ± 5.91	38.83 ± 9.74	no
239.95 ± 43.25	35.05 ± 6.32	40.88 ± 10.31	no
250.31 ± 51.06	36.56 ± 7.46	40.45 ± 10.29	no
251.47 ± 53.96	36.73 ± 7.88	40.51 ± 10.24	no
253.08 ± 47.81	36.96 ± 6.98	41.74 ± 10.85	no
253.08 ± 45.29	36.96 ± 6.62	39.78 ± 10.12	no
253.18 ± 58.35	36.98 ± 8.52	39.86 ± 10.26	no
262.37 ± 51.25	38.32 ± 7.49	35.76 ± 10.01	yes
264.96 ± 65.51	38.70 ± 9.57	35.89 ± 8.88	yes
274.02 ± 85.98	40.02 ± 12.56	38.42 ± 9.85	yes

^{a}A horizontal line differentiates the productive simulations from the unproductive ones. A higher kinetic energy is essential to overcome the hydrogen bond constraint. As in Set-1, the increase in average kinetic energy of the system supports greater propensity for a productive simulation. The transition point in this respect appears to be between 36.98 and 38.32 kcal/mol (higher than that for Set-1). Also note that the system potential energy is higher (and hence less stable) for the unproductive simulations here. ^{b}Potential energy change during the simulation. As already noted in Table 4, the unproductive simulations have a higher potential energy compared to the productive ones. In addition, the productive simulations here have an average potential energy that is roughly 10−13 kcal/mol higher as compared to the ones in Table 4. These aspects are also witnessed in Figure 13ii. ^{c}Computed from the nuclear kinetic energy using the equipartition theorem $(3/2(N - 1)kT)$.

an effective Lagrangian, surrogate degrees of freedom are introduced that couple to a selection of system variables. The dynamics

N

dx.doi.org/10.1021/jp3015047 | J. Phys. Chem. B XXXX, XXX, XXX−XXX
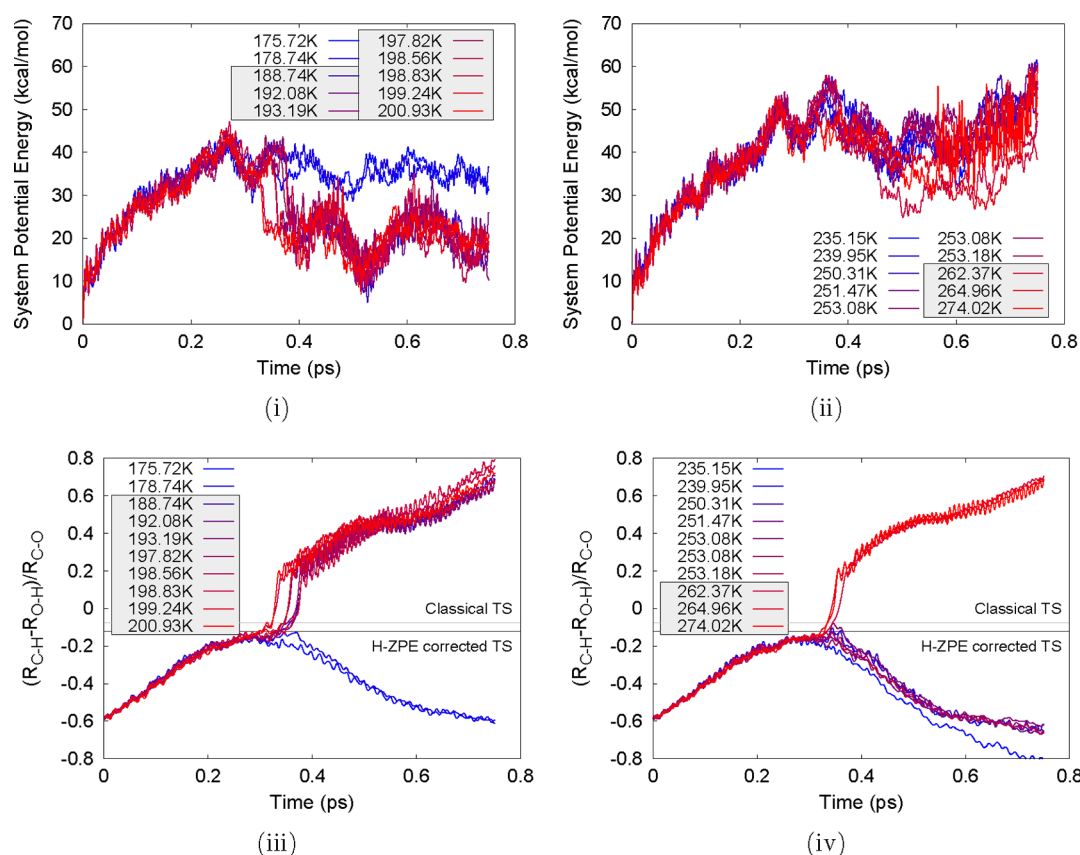
Figure 13. Evolution of system potential energy for Model-1: (i) unconstrained (Set-1) and (ii) Ile839 constrained (Set-2). Evolution of RC = $(R_{CH} - R_{OH})/R_{CO}$ for Model-1: (iii) unconstrained (Set-1) and (iv) Ile839 constrained (Set-2). The color code for all cases is chosen such that red indicates the warmer simulations as compared with blue. Also, gray boxes are drawn in the legend to signify temperatures that yield productive simulations. Except the two lowest temperature simulations where the hydrogen transfer is inhibited, all other unconstrained simulations (Set-1) follow a lower potential energy path in the transfer process as compared to the constrained, mostly unproductive simulations of Set-2. Thus, the lower energy product state is only visited when the constraint in Ile839 is released in Model-1. The horizontal lines represent the classical transition state (RC = −0.078) and hydrogen nuclear zero point energy (H-ZPE) corrected transition state (RC = −0.121) obtained from the previous quantum dynamics study.[7]

of these bath variables then triggers the sampling of rare events through the aforementioned coupling term. Furthermore, the effective electron−nuclear Lagrangian is couched within an atom-centered localized basis formalism for electronic structure that allows the direct utilization of advanced density functionals. The approach is also cast within a QM/MM framework to facilitate the treatment of large systems such as enzymes.

The method is utilized to probe the effect of active site dynamical fluctuations, or ensemble sampling, in facilitating the critical hydrogen transfer step in the SLO-1 catalyzed oxidation of linoleic acid. The effect of these active site fluctuations is gauged and controlled through structural constraints enforced on the dynamics. Within an experimental setting, these constraints are generally enforced through amino acid mutations. It is found here that these constraints limit the electrostatic fluctuations within the active site, thus having a negative impact on the transfer process. None of the constraints studied here enhanced the transfer process. The precise effect on the hydrogen transfer reaction is quantitatively scrutinized using an active site structure flexibility index introduced here from the principal dynamical components obtained from the trajectory. Such a flexibility index turns out to have a direct correspondence to the effectiveness of the transfer process.

These results on the importance of structural flexibility in enzyme reactions are complementary to other discussions[147−155]

involving the relation between protein dynamics and enzyme catalysis. In fact, this is a hot debate issue in enzymology.[147−155] The work presented here has the critical feature of including the electronic effects within the dynamics, as this generally has a polarizing role on the nuclear dynamics and the reactive process.

■ APPENDIX A: NUMERICAL BENCHMARKS ON THE DYNAMICS OBTAINED USING EQ 2

Here, we probe the energy conservation properties for the rare event sampling methodology described in section II. To simplify the analysis, we have chosen to model the proton transfer in the phenol-trimethyl-amine, $PhOH-N(CH_3)_3$, system. This cluster is expected to be a good candidate for our methodology, since the time scale for the proton to transfer from the donor-oxygen to acceptor-nitrogen is large, because the potential barrier in the gas phase is ≈25 kcal/mol and the product state is an unstable zwitterion. For the simulations described in this section, we tethered a bath particle to the shared hydrogen with a force constant of 15570 pN/Å (~224.10 kcal/mol·Å²) and performed the dynamics with both Born−Oppenheimer molecular dynamics (BOMD)[4,5,11,61,209−213] and atom centered density matrix propagation (ADMP)[61,108−110] approaches at the level of B3LYP/6-31+G(d,p). The BOMD method differs from ADMP
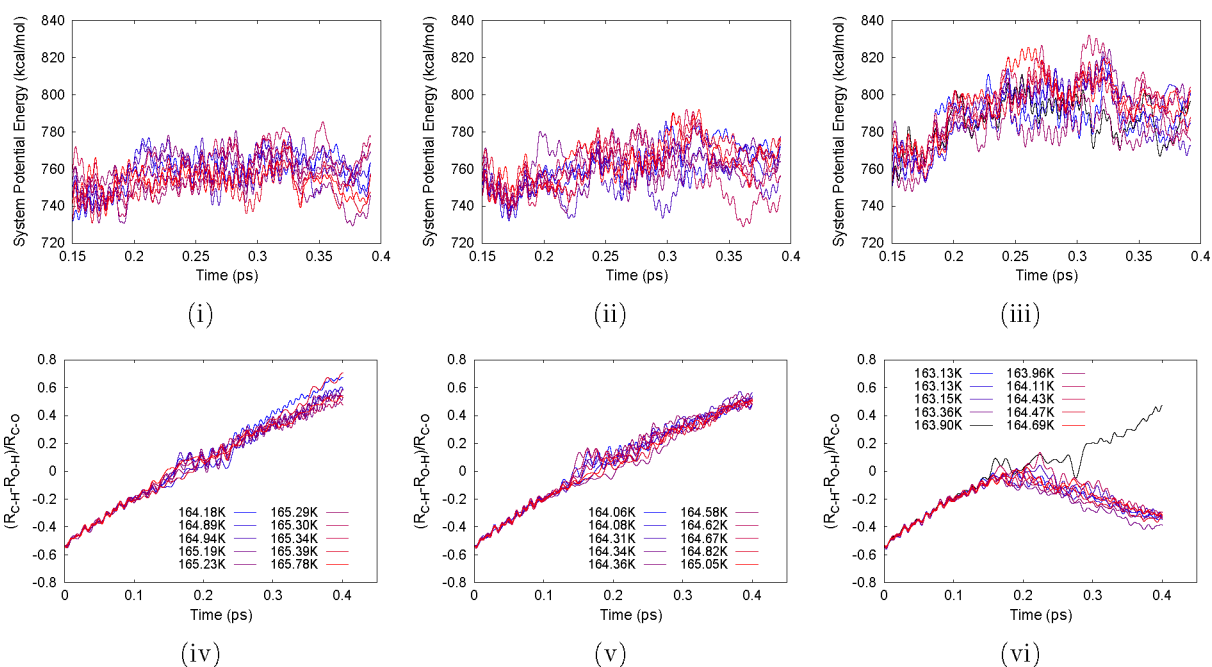
Figure 14. The figure displays the evolution of the system potential energy evolution for Model-2: (i) unconstrained (Set-1), (ii) Ile839 constrained (Set-2), and (iii) active site constrained (Set-3). The evolution of $RC = (R_{CH} - R_{OH})/R_{CO}$ for Model-2 is presented in (iv) Set-1, (v) Set-2, and (vi) Set-3. As noted in Figure 13, the color code is chosen such that red indicates warmer simulations as compared with the blue trajectories. The only exception is Set-3 where the single productive run is shown in black. For Model-2, the hydrogen transfer occurs 100% for Set-1 and Set-2 simulations, while, for Set-3, the transfer is inhibited in 90% of the simulations. Furthermore, the potential energy landscape traversed during Set-3 is higher as compared to Set-1 and Set-2. Upon inspection of Tables 6 and 7, it may also be noted that this is the case also for Set-2 relative to Set-1.

in that the electronic structure is converged at every step as opposed to being propagated through the extended Lagrangian described in the main portion of this publication. Thus, the benchmark presented here also serves the purpose of comparison between these to approaches, although more extensive comparisons can be found elsewhere.[109,111] The choice of mass for the bath degree of freedom was based on the fact that the largest reduced mass of the normal modes is ≈7 amu, and we would like the dynamics of the bath to be well separated from the time scale of the other molecular vibrations.

In Table 3, we show the energy conservation data for each simulation performed. The energy of the entire system [$\mathcal{H}_{system} + \mathcal{H}_{bath}$; see eqs 18–20] is conserved to within a hundredth of a kcal/mol.

The effectiveness of the simulations for biasing the sampling of the acceptor moiety is clearly demonstrated in Figure 12, which displays the reduced reaction coordinate, $(R_{OH} - R_{NH})/R_{ON}$, as a function of time. In this figure, we note that the sampling occurs rather rapidly for the biased trajectories, whereas the unbiased trajectory oscillates about the initial configuration. We also notice that the more massive fictitious degrees of freedom allowed for a slower transfer process, thus allowing more extensive sampling of the configuration space during the process. These factors have been used in the main publication to determine appropriate values for the bath degrees of freedom as well as coupling potential force constants.

■ APPENDIX B: GAUGING THE STATISTICAL FLUCTIATIONS IN THE RARE EVENTS STUDIES THROUGH SIMULATIONS AT MULTIPLE TEMPERATURES

To confirm the rare events results, we carried out multiple simulations by varying initial conditions for Model-1 (Set-1 and Set-2) and for Model-2 (Set-1, Set-2, and Set-3). The individual simulations within each set differed in the randomized seed provided to compute the initial nuclear and electronic density matrix velocities.[6,108,109,111,113–119,121,122] Specifically, the initial values for each component of the velocities for the nuclear and electronic variables are chosen at random under the condition that the total initial kinetic energy provided to the system is the same for all simulations in a given set. This ensures a Boltzman distribution[113,117–119,121] of initial velocities for the starting configuration. A summary of results for Model-1 is presented in Table 4 (for Set-1) and Table 5 (for Set-2). The evolution of RC is presented in Figure 13. As noted in Tables 4 and 5, the hydrogen transfer occurs in 80% of the Model-1, Set-1 simulations and 30% of the simulations for Set-2 (see Figure 13iii and iv). While parallel tempering[214–216] trajectories can be constructed on the basis of the simulations listed, it is already clear that the statistically averaged trajectory for Set-1 favors a hydrogen transfer, while that for Set-2 does not. The general trends here are thus in support of the results presented in section IIIB1 of the manuscript. Compare Figure 13iii and iv with the RC values plotted in black in the top panels of Figure 7. The data in Figure 7 present a trend that is consistent with that in Figure 13. In addition, as noted in Tables 4 and 5, the effective system kinetic energy required to promote hydrogen transfer in the constrained Set-2 simulations appears to be approximately 10 kcal/mol higher as compared to that in Set-1. The higher temperature is necessary to overcome the absence of hydrogen bonding flexibility in Set-2. Furthermore, as seen from Figure 13i and ii, the higher average kinetic energy of the productive Set-2 simulations results in higher potential, less stable acceptor-bound configurations. Thus, constraining the hydrogen bond in Model-1 hinders the transfer process and, for cases where such a hindrance can be overcome by providing a higher system kinetic energy (or temperature), the resultant acceptor-bound

Table 6. Summary of Simulations for Model-2: Set-1

system nuclear kinetic energy (average ± rms)		system potential energy[a] (average ± rms)	
Kelvin[b]	kcal/mol	kcal/mol	transfer?
164.18 ± 11.12	1063.43 ± 72.01	751.59 ± 74.59	yes
164.89 ± 11.61	1068.05 ± 75.21	754.44 ± 77.57	yes
164.94 ± 11.72	1068.38 ± 75.94	752.92 ± 77.73	yes
165.19 ± 11.23	1069.97 ± 72.72	753.72 ± 74.72	yes
165.23 ± 11.36	1070.24 ± 73.57	748.38 ± 75.11	yes
165.29 ± 11.59	1070.67 ± 75.09	752.17 ± 76.48	yes
165.30 ± 11.53	1070.71 ± 74.66	752.59 ± 77.14	yes
165.34 ± 11.43	1070.99 ± 74.03	756.45 ± 75.36	yes
165.39 ± 11.38	1071.28 ± 73.74	747.74 ± 74.43	yes
165.78 ± 11.89	1073.83 ± 77.04	751.19 ± 77.95	yes

[a]Potential energy change during the simulation. [b]Computed from the nuclear kinetic energy using the equipartition theorem $(3/2(N-1)kT)$.

Table 7. Summary of Simulations for Model-2: Set-2

system nuclear kinetic energy (average ± rms)		system potential energy[a] (average ± rms)	
Kelvin[b]	kcal/mol	kcal/mol	transfer?
164.06 ± 11.22	1062.70 ± 72.69	756.50 ± 75.75	yes
164.08 ± 11.31	1062.79 ± 73.28	752.22 ± 76.77	yes
164.31 ± 10.88	1064.26 ± 70.47	749.11 ± 72.69	yes
164.34 ± 12.10	1064.46 ± 78.36	757.61 ± 80.57	yes
164.36 ± 11.21	1064.59 ± 72.58	752.90 ± 74.77	yes
164.58 ± 10.85	1066.03 ± 70.31	758.45 ± 72.98	yes
164.62 ± 11.70	1066.30 ± 75.81	750.18 ± 77.35	yes
164.67 ± 11.38	1066.66 ± 73.69	755.29 ± 76.22	yes
164.82 ± 11.63	1067.63 ± 75.32	758.11 ± 78.13	yes
165.05 ± 11.45	1069.09 ± 74.19	756.66 ± 77.01	yes

[a]Potential energy change during the simulation. [b]Computed from the nuclear kinetic energy using the equipartition theorem $(3/2(N-1)kT)$.

Table 8. Summary of Simulations for Model-2: Set-3[a]

system nuclear kinetic energy (average ± rms)		system potential energy[a] (average ± rms)	
Kelvin[b]	kcal/mol	kcal/mol	transfer?
163.13 ± 11.57	1056.64 ± 74.95	768.98 ± 83.86	no
163.13 ± 11.47	1056.66 ± 74.31	772.57 ± 82.60	no
163.15 ± 11.37	1056.80 ± 73.66	770.60 ± 82.30	no
163.36 ± 11.59	1058.17 ± 75.06	775.56 ± 84.66	no
163.90 ± 11.35	1061.66 ± 73.54	769.31 ± 81.75	yes
163.96 ± 11.25	1062.00 ± 72.89	764.42 ± 79.69	no
164.11 ± 11.45	1063.01 ± 74.14	775.74 ± 83.86	no
164.43 ± 11.47	1065.08 ± 74.29	775.64 ± 84.35	no
164.47 ± 11.45	1065.31 ± 74.19	773.27 ± 83.68	no
164.69 ± 10.92	1066.75 ± 70.75	779.44 ± 79.64	no

[a]The behavior of the average system potential energy for the unproductive simulations relative to the productive trajectories is similar to that noted in Model-1. [a]Potential energy change during the simulation. [b]Computed from the nuclear kinetic energy using the equipartition theorem $(3/2(N-1)kT)$.

species are not as stable as those found in cases where the hydrogen bond formation is not inhibited. This implies that the average potential energy barrier traversed during the transfer process is lower for Set-1 than for Set-2 and the hydrogen bond in Model-1 has a critical role in the transfer process as already concluded in section IIIB1 of the paper.

In the case of Model-2, the trajectory summary is presented in Table 6 for Set-1, Table 7 for Set-2, and Table 8 for Set-3. Here, the hydrogen transfer occurs in all simulations for Set-1 and Set-2 but only in one of the higher temperature simulations for Set-3. Thus, the simulations strongly support the representative results presented in section IIIB2.

In agreement with the observations for Model-1, the system potential energy for Model-2 (relative to its starting value) is also significantly lower for Set-1 and Set-2 as compared to Set-3 where the active site is constrained (compare Tables 6−8). Furthermore, although the Set-2 simulations are productive, the average potential energies here are about 5 kcal/mol higher than those in Set-1. This is an indication that the unconstrained simulations (Set-1) follow a lower energy barrier as compared to the constrained trajectories. It is also useful to note that the productive Set-1 and Set-2 simulations have donor−acceptor distances in the range of 2.67 ± 0.4 to 2.71 ± 0.4 Å. By contrast, the Set-3 simulations that are nonproductive as a result of the active site structural constraints have donor−acceptor distances in a higher range of 2.70 ± 0.4 to 2.75 ± 0.4 Å. Thus, the donor−acceptor gating mode is also restricted by the applied structural constraints, although the constraints that hinder flexibility are not directly applied on the donor and acceptor atoms.

■ ASSOCIATED CONTENT

Ⓢ Supporting Information

Additional information, figures, and tables on Model-2: probing the effect of the active site using asymptotic boundary conditions, including estimating the effect of constraints on the 14 Å subsystem and analysis of fluctuations. This material is available free of charge via the Internet at http://pubs.acs.org.

■ AUTHOR INFORMATION

Corresponding Author
*E-mail: iyengar@indiana.edu.
Notes
The authors declare no competing financial interest.

■ ACKNOWLEDGMENTS

■ REFERENCES

(1) Hynes, J. T., Klinman, J. P., Limbach, H.-H., Schowen, R. L., Eds. *Hydrogen-Transfer Reactions*; Wiley-VCH: Weinheim, 2007.
(2) Isaacs, N. *Physical Organic Chemistry*; Wiley & Sons: New York, 1995.
(3) Sheridan, R.; *Reviews Of Reactive Intermediate Chemistry*. Wiley-Interscience: Hoboken, NJ, 2007; Chapter Quantum Mechanical Tunneling In Organic Reactive Intermediates.
(4) Payne, M. C.; Teter, M. P.; Allan, D. C.; Arias, T. A.; Joannopoulos, J. D. *Rev. Mod. Phys.* **1992**, *64*, 1045−1097.
(5) Deumens, E.; Diz, A.; Longo, R.; Öhrn, Y. *Rev. Mod. Phys.* **1994**, *66*, 917−983.
(6) Rega, N.; Iyengar, S. S.; Voth, G. A.; Schlegel, H. B.; Vreven, T.; Frisch, M. J. *J. Phys. Chem. B* **2004**, *108*, 4210−4220.
(7) Iyengar, S. S.; Sumner, I.; Jakowski, J. *J. Phys. Chem. B* **2008**, *112*, 7601−7613.
(8) Sumner, I.; Iyengar, S. S. *J. Chem. Phys.* **2008**, *129*, 054109.
(9) Sumner, I.; Iyengar, S. S. *J. Chem. Theory Comput.* **2010**, *6*, 1698.
(10) Laio, A.; VandeVondele, J.; Röthlisberger, U. *J. Chem. Phys.* **2002**, *116*, 6941−6947.

(11) Car, R.; Parrinello, M. *Phys. Rev. Lett.* **1985**, *55*, 2471−2474.

(12) Toniolo, A.; Granucci, G.; Martinez, T. J. *J. Phys. Chem. A* **2003**, *107*, 3822−3830.

(13) Gao, J. *Acc. Chem. Res.* **1996**, *29*, 298.

(14) Eichinger, M.; Tavan, P.; Hutter, J.; Parrinello, M. *J. Chem. Phys.* **1999**, *110*, 10452.

(15) Pu, J. Z.; Gao, J. L.; Truhlar, D. G. *Chem. Rev.* **2006**, *106*, 3140−3169.

(16) Gao, J. L.; Ma, S. H.; Major, D. T.; Nam, K.; Pu, J. Z.; Truhlar, D. G. *Chem. Rev.* **2006**, *106*, 3188−3209.

(17) Benkovic, S. J.; Hammes-Schiffer, S. *Science* **2006**, *312*, 208.

(18) Bolhuis, P. G.; Dellago, C.; Chandler, D.; Geissler, P. *Annu. Rev. Phys. Chem.* **2002**, *59*, 291.

(19) Warshel, A.; Sharma, P.; Kato, M.; Xiang, Y.; Liu, H.; Olsson, M. *Chem. Rev.* **2006**, *106* (8), 3210−3235.

(20) Nagel, Z.; Klinman, J. *Chem. Rev.* **2006**, *106* (8), 3095−3118.

(21) Antoniou, D.; Basner, J.; Nunez, S.; Schwartz, S. *Chem. Rev.* **2006**, *106* (8), 3170−3187.

(22) Warshel, A. *Computer Modeling Of Chemical Reactions In Enzymes And Solutions*; John Wiley & Sons, Inc.: New York, 1997.

(23) Siebrand, W.; Smedarchina, Z. *J. Phys. Chem. B* **2004**, *108*, 4185.

(24) Tejero, I.; Garcia-Viloca, M.; Gonzalez-Lafont, A.; Lluch, J. M.; York, D. M. *J. Phys. Chem. B* **2006**, *110*, 24708.

(25) Ayton, G. S.; Lyman, E.; Voth, G. A. *Faraday Discuss.* **2010**, *144*, 347−357.

(26) Joshi, H.; Singharoy, A.; Sereda, Y. V.; Cheluvaraja, S. C.; Ortoleva, P. J. *Prog. Biophys. Mol. Biol.* **2011**, *107*, 200−217.

(27) Park, S.; Khalili-Araghi, F.; Tajkhorshid, E.; Schulten, K. *J. Chem. Phys.* **2003**, *119*, 3559−3566.

(28) Park, S.; Schulten, K. *J. Chem. Phys.* **2004**, *120*, 5946−5961.

(29) Arkhipov, A.; Freddolino, P. L.; Imada, K.; Namba, K.; Schulten, K. *Biophys. J.* **2006**, *91*, 4589−4597.

(30) Izvekov, S.; Voth, G. A. *J. Phys. Chem. B* **2005**, *109*, 2469−2473.

(31) Miller, T. F.; Vanden-Eijnden, E.; Chandler, D. *Proc. Natl. Acad. Sci. U.S.A.* **2007**, *104*, 14559−14564.

(32) Maragakis, P.; Lindorff-Larsen, K.; Eastwood, M. P.; Dror, R. O.; Klepeis, J. L.; Arkin, I. T.; Jensen, M. O.; Xu, H.; Trbovic, N.; Friesner, R. A.; Palmer, A. G., III; Shaw, D. E. *J. Phys. Chem. B* **2008**, *112* (19), 6155−6158.

(33) Olsson, M. H. M.; Parson, W. W.; Warshel, A. *Chem. Rev.* **2006**, *106*, 1737−1756.

(34) Hammes-Schiffer, S.; Benkovic, S. J. *Annu. Rev. Biochem.* **2006**, *75*, 519.

(35) Liang, Z. X.; Klinman, J. P. *Curr. Opin. Struct. Biol.* **2004**, *14*, 648.

(36) Klinman, J. P. *Pure Appl. Chem.* **2003**, *75*, 601.

(37) Knapp, M. J.; Rickert, K.; Klinman, J. P. *J. Am. Chem. Soc.* **2002**, *124*, 3865.

(38) Glickman, M. H.; Wiseman, J. S.; Klinman, J. P. *J. Am. Chem. Soc.* **1994**, *116*, 793.

(39) Jonsson, T.; Glickman, M. H.; Sun, S. J.; Klinman, J. P. *J. Am. Chem. Soc.* **1996**, *118*, 10319.

(40) Lehnert, N.; Solomon, E. I. *J. Biol. Inorg. Chem.* **2003**, *8*, 294.

(41) Hatcher, E.; Soudackov, A. V.; Hammes-Schiffer, S. *J. Am. Chem. Soc.* **2004**, *126*, 5763−5775.

(42) Olsson, M. H. M.; Siegbahn, P. E. M.; Warshel, A. *J. Am. Chem. Soc.* **2004**, *126*, 2820−2828.

(43) Jarzynski, C. *Annu. Rev. Condens. Matter Phys.* **2011**, *2*, 329−351.

(44) Jarzynski, C. *Phys. Rev. Lett.* **1997**, *78* (14), 2690−2693.

(45) Jarzynski, C. *Phys. Rev. E* **1997**, *56*, 5018−5035.

(46) Ilan, B.; Tajkhorshid, E.; Schulten, K.; Voth, G. A. *Proteins: Struct., Funct., Bioinf.* **2004**, *55*, 223−228.

(47) Presse, S.; Silbey, R. *J. Chem. Phys.* **2006**, *124*, 054117.

(48) Presse, S.; Silbey, R. *J. Phys. Rev. E* **2006**, *74*, 061105.

(49) Liphardt, J.; Dumont, S.; Smith, S.; Tinoco, I.; Bustamante, C. *Science* **2002**, *296*, 1832−1835.

(50) MacFadyen, J.; Andricioaei, I. *J. Chem. Phys.* **2005**, *123*, 074107.

(51) Park, S.; Schulten, K. *J. Chem. Phys.* **2004**, *120*, 5946.

(52) Paci, E.; Karplus, M. *J. Mol. Biol.* **1999**, *288*, 441.

(53) Ensing, B.; Laio, A.; Parrinello, M.; Klein, M. L. *J. Phys. Chem. B* **2005**, *109*, 6676−6687.

(54) Abrams, J. B.; Tuckerman, M. E. *J. Phys. Chem. B* **2008**, *112*, 15742−15757.

(55) Maragliano, L.; Vanden-Eijnden, E. *Chem. Phys. Lett.* **2006**, *426*, 168−175.

(56) Andersen, H. C. *J. Chem. Phys.* **1980**, *72*, 2384−2393.

(57) Parrinello, M.; Rahman, A. *Phys. Rev. Lett.* **1980**, *45*, 1196−1199.

(58) Nosé, S. *J. Chem. Phys.* **1984**, *81*, 511.

(59) Hoover, W. G. *Phys. Rev. A* **1985**, *31*, 1695−1697.

(60) Car, R.; Parrinello, M. *Phys. Rev. Lett.* **1985**, *55*, 2471−2474.

(61) Schlegel, H. B.; Millam, J. M.; Iyengar, S. S.; Voth, G. A.; Daniels, A. D.; Scuseria, G. E.; Frisch, M. J. *J. Chem. Phys.* **2001**, *114*, 9758−9763.

(62) Cukier, R. I.; Deutch, J. M. *Phys. Rev.* **1969**, *177*, 240.

(63) Krylov, N.; Bogoliubov, N. N. *Introduction to Nonlinear Mechanics*; Princeton University Press: Princeton, NJ, 1947.

(64) Bender, C. M.; Orzag, S. A. *Advanced Mathematical Methods for Scientists and Engineers*; McGraw-Hill Publishing Company: New York, 1978.

(65) Pavese, M.; Berard, D. R.; Voth, G. A. *Chem. Phys. Lett.* **1999**, *300*, 93−98.

(66) Marx, D.; Tuckerman, M. E.; Martyna, G. J. *Comput. Phys. Commun.* **1999**, *118*, 166.

(67) Li, X.; Iyengar, S. S. *J. Chem. Phys.* **2010**, *133*, 184105.

(68) Feynman, R. P. *Statistical Mechanics*; Addison-Wesley: Reading, MA, 1972.

(69) Feynman, R. P.; Hibbs, A. R. *Quantum Mechanics and Path Integrals*; McGraw-Hill Book Company: New York, 1965.

(70) Tuckerman, M. E.; Marx, D.; Klein, M. L.; Parrinello, M. *J. Chem. Phys.* **1996**, *104*, 5579−5588.

(71) Chandler, D.; Wolynes, P. G. *J. Chem. Phys.* **1981**, *74*, 4078.

(72) Wong, K. Y.; Gao, J. *J. Chem. Phys.* **2007**, *127*, 211103.

(73) Wong, K. Y.; Gao, J. *J. Chem. Theory Comput.* **2008**, *4*, 1409−1422.

(74) Olender, R.; Elber, R. *J. Chem. Phys.* **1996**, *105*, 9299.

(75) Elber, R.; Ghosh, A.; Cardenas, A. *Acc. Chem. Res.* **2002**, *35*, 396−403.

(76) Elber, R.; Ghosh, A.; Cardenas, A. In *Bridging the time scales: molecular simulations for the next decade*; Nielaba, P., Mareschal, M., Ciccotti, G., Eds.; Springer Verlag: Berlin, 2002; Chapter The Stochastic Difference Equation as a tool to compute long time dynamics, pp 335−363.

(77) Elber, R.; Ghosh, A.; Cardenas, A.; Stern, H. *Adv. Chem. Phys.* **2003**, *126*, 93−129.

(78) Elber, R. *Curr. Opin. Struct. Biol.* **2005**, *15*, 151−156.

(79) Passerone, D.; Parrinello, M. *Phys. Rev. Lett.* **2001**, *87* (10), 108302.

(80) Passerone, D.; Ceccarelli, M.; Parrinello, M. *J. Chem. Phys.* **2003**, *118* (5), 2025−2032.

(81) Dellago, C.; Bolhuis, P. G.; Csajka, F. S.; Chandler, D. *J. Chem. Phys.* **1998**, *108* (5), 1964−1977.

(82) Elber, R.; Karplus, M. *Chem. Phys. Lett.* **1987**, *139* (5), 375−380.

(83) Gillilan, R. E.; Wilson, K. R. *J. Chem. Phys.* **1992**, *97*, 1757−1772.

(84) Henkelman, G.; Jonsson, H. *J. Chem. Phys.* **2000**, *113*, 9978−9985.

(85) Sørensen, M. R.; Voter, A. F. *J. Chem. Phys.* **2000**, *112*, 9599.

(86) Carter, E. A.; Ciccotti, G.; Hynes, J. T.; Kapral, R. *Chem. Rev. Lett.* **1989**, *156*, 472.

(87) Voter, A. F. *J. Chem. Phys.* **1997**, *106*, 4665.

(88) Voter, A. F. *Phys. Rev. Lett.* **1997**, *78*, 3908.

(89) Zuckerman, D. M. *Annu. Rev. Biophys.* **2011**, *40*, 187−203.

(90) Barducci, A.; Bonomi, M.; Parrinello, M. *Wiley Interdiscip. Rev.: Comput. Mol. Sci.* **2011**, *1*, 826−843.

(91) Ozer, G.; Valeev, E. F.; Quirk, S.; Hernandez, R. *J. Chem. Theory Comput.* **2010**, *6*, 3026−3038.

(92) Warshel, A.; Levitt, M. *J. Mol. Biol.* **1976**, *103*, 227.

(93) Singh, U. C.; Kollman, P. A. *J. Comput. Chem.* **1986**, *7*, 718.

(94) Field, C.; Bash, P. A.; Karplus, M. *J. Comput. Chem.* **1990**, *11*, 700.

(95) Maseras, F.; Morokuma, K. *J. Comput. Chem.* **1995**, *16*, 1170−1179.

(96) Ferenczy, G. G.; Rivail, J.-L.; Surjan, P. R.; Naray-Szabo, G. *J. Comput. Chem.* **1992**, *13*, 830.

(97) Gao, J.; Amara, P.; Alhambra, C.; Field, M. *J. Phys. Chem. A* **1998**, *102*, 4714.

(98) Zhang, Y.; Lee, T.-S.; Yang, W. *J. Chem. Phys.* **1999**, *110*, 45.

(99) Stanton, R. V.; Hartsough, D. S.; Merz, K. M. *J. Comput. Chem.* **1994**, *16*, 113.

(100) Alhambra, C., Byun, K., Gao, J. In *Combined Quantum Mechanical and Molecular Mechanics Methods*; Gao, J., Thompson, M., Eds.; ACS Symposium Series No. 712; American Chemical Society: Washington, DC, 1999; p 35.

(101) Reuter, N.; Dejaegere, A.; Maigret, B.; Karplus, M. *J. Phys. Chem. A* **2000**, *104*, 1720.

(102) Murphy, R. B.; Philipp, D. M.; Friesner, R. A. *J. Comput. Chem.* **2000**, *21*, 1442.

(103) Woo, T. K.; Margl, P. M.; Deng, L.; Ziegler, T. In *Combined Quantum Mechanical and Molecular Mechanics Methods*; Gao, J., Thompson, M., Eds.; ACS Symposium Series No. 712; American Chemical Society: Washington, DC, 1999; p 128.

(104) Gordon, M. S.; Freitag, M. A.; Bandyopadhyay, P.; Jensen, J. H.; Kairys, V.; Stevens, W. J. *J. Phys. Chem. A* **2001**, *105*, 293−307.

(105) Zhang, Y.; Lin, H.; Truhlar, D. *J. Chem. Theory Comput.* **2007**, *3* (4), 1378−1398.

(106) Lin, H.; Truhlar, D. G. *Theor. Chem. Acc.* **2007**, *117*, 185−199.

(107) Hratchian, H. P.; Parandekar, P. V.; Raghavachari, K.; Frisch, M. J.; Vreven, T. *J. Chem. Phys.* **2008**, *128*, 034107.

(108) Iyengar, S. S.; Schlegel, H. B.; Millam, J. M.; Voth, G. A.; Scuseria, G. E.; Frisch, M. J. *J. Chem. Phys.* **2001**, *115*, 10291−10302.

(109) Schlegel, H. B.; Iyengar, S. S.; Li, X.; Millam, J. M.; Voth, G. A.; Scuseria, G. E.; Frisch, M. J. *J. Chem. Phys.* **2002**, *117*, 8694−8704.

(110) Iyengar, S. S.; Schlegel, H. B.; Voth, G. A.; Millam, J. M.; Scuseria, G. E.; Frisch, M. J. *Isr. J. Chem.* **2002**, *42*, 191−202.

(111) Iyengar, S. S.; Frisch, M. J. *J. Chem. Phys.* **2004**, *121*, 5061−5070.

(112) Iyengar, S. S.; Schlegel, H. B.; Voth, G. A. *J. Phys. Chem. A* **2003**, *107*, 7269−7277.

(113) Iyengar, S. S.; Petersen, M. K.; Day, T. J. F.; Burnham, C. J.; Teige, V. E.; Voth, G. A. *J. Chem. Phys.* **2005**, *123*, 084309.

(114) Iyengar, S. S. *J. Chem. Phys.* **2007**, *126*, 216101.

(115) Iyengar, S. S.; Day, T. J. F.; Voth, G. A. *Int. J. Mass Spectrom.* **2005**, *241*, 197−204.

(116) Iyengar, S. S. *J. Chem. Phys.* **2005**, *123*, 084310.

(117) Li, X.; Teige, V. E.; Iyengar, S. S. *J. Phys. Chem. A* **2007**, *111*, 4815−4820.

(118) Li, X.; Moore, D. T.; Iyengar, S. S. *J. Chem. Phys.* **2008**, *128*, 184308.

(119) Li, X.; Oomens, J.; Eyler, J. R.; Moore, D. T.; Iyengar, S. S. *J. Chem. Phys.* **2010**, *132*, 244301.

(120) Vimal, D.; Pacheco, A. B.; Iyengar, S. S.; Stevens, P. S. *J. Phys. Chem. A* **2008**, *112*, 7227−7237.

(121) Pacheco, A. B.; Dietrick, S. M.; Stevens, P. S.; Iyengar, S. S. *J. Phys. Chem. A* **2012**, *116*, 4108.

(122) Dietrick, S. M.; Pacheco, A. B.; Phatak, P.; Stevens, P. S.; Iyengar, S. S. *J. Phys. Chem. A* **2012**, *116*, 399−414.

(123) Swope, W. C.; Andersen, H. C.; Berens, P. H.; Wilson, K. R. *J. Chem. Phys.* **1982**, *76*, 637−649.

(124) Bakowies, D.; Thiel, W. *J. Phys. Chem.* **1996**, *100*, 10580.

(125) Svensson, M.; Humbel, S.; Froese, R. D. J.; Matsubara, T.; Sieber, S.; Morokuma, K. *J. Phys. Chem.* **1996**, *100*, 19357.

(126) Vreven, T.; Morokuma, K. *J. Comput. Chem.* **2000**, *21*, 1419−1432.

(127) Vreven, T.; Morokuma, K.; Farkas, O.; Schlegel, H. B.; Frisch, M. J. *J. Comput. Chem.* **2003**, *24*, 760.

(128) Vreven, T.; Morokuma, K. *Theor. Chem. Acc.* **2003**, *109*, 125.

(129) McWeeny, R. *Rev. Mod. Phys.* **1960**, *32*, 335.

(130) Golub, G. H.; Loan, C. F. V. *Matrix Computations*; The Johns Hopkins University Press: Baltimore, MD, 1996.

(131) Helgaker, T.; Jørgensen, P.; Olsen, J. *Molecular Electronic-Structure Theory*; John Wiley and Sons, Ltd.: New York, 2000.

(132) Mayo, S. L.; Olafson, B. D.; Goddard, W. A. *J. Phys. Chem.* **1990**, *94*, 8897.

(133) Li, Y.; Zhu, F.; Vaidehi, N.; W. A. Goddard, I. *J. Am. Chem. Soc.* **2007**, *129*, 10720.

(134) Maseras, F. *Chem. Commun.* **2000**, *19*, 1821.

(135) Tao, J.; Perdew, J. P.; Staroverov, V. N.; Scuseria, G. E. *Phys. Rev. Lett.* **2003**, *91*, 146401.

(136) Zhao, Y.; Truhlar, D. G. *J. Phys. Chem. A* **2004**, *108*, 6908.

(137) Maximoff, S. N.; Ernzerhof, M.; Scuseria, G. E. *J. Chem. Phys.* **2004**, *120*, 2105−2109.

(138) Scuseria, G. E. *J. Phys. Chem. A* **1999**, *103*, 4782.

(139) Frisch, M. J.; Trucks, G. W.; Schlegel, H. B.; Scuseria, G. E.; Robb, M. A.; Cheeseman, J. R.; Montgomery, J. A., Jr.; Vreven, T.; Scalmani, G.; Kudin, K. N.; Iyengar, S. S.; Tomasi, J.; Barone, V.; Mennucci, B.; Cossi, M.; Rega, N.; Petersson, G. A.; Nakatsuji, H.; Hada, M.; Ehara, M.; Toyota, K.; Fukuda, R.; Hasegawa, J.; Ishida, M.; Nakajima, T.; Honda, Y.; Kitao, O.; Nakai, H.; Li, X.; Hratchian, H. P.; Peralta, J. E.; Izmaylov, A. F.; Brothers, E.; Staroverov, V.; Kobayashi, R.; Normand, J.; Burant, J. C.; Millam, J. M.; Klene, M.; Knox, J. E.; Cross, J. B.; Bakken, V.; Adamo, C.; Jaramillo, J.; Gomperts, R.; Stratmann, R. E.; Yazyev, O.; Austin, A. J.; Cammi, R.; Pomelli, C.; Ochterski, J. W.; Ayala, P. Y.; Morokuma, K.; Voth, G. A.; Salvador, P.; Dannenberg, J. J.; Zakrzewski, V. G.; Dapprich, S.; Daniels, A. D.; Strain, M. C.; Farkas, O.; Malick, D. K.; Rabuck, A. D.; Raghavachari, K.; Foresman, J. B.; Ortiz, J. V.; Cui, Q.; Baboul, A. G.; Clifford, S.; Cioslowski, J.; Stefanov, B. B.; Liu, G.; Liashenko, A.; Piskorz, P.; Komaromi, I.; Martin, R. L.; Fox, D. J.; Keith, T.; Al-Laham, M. A.; Peng, C. Y.; Nanayakkara, A.; Challacombe, M.; Chen, W.; Wong, M. W.; Pople, J. A. *Gaussian development version*, revision e.05; Wallingford, CT, 2006.

(140) Goldstein, H.; Poole, C.; Safko, J. *Classical Mechanics*; Addison Wesley: San Francisco, CA, 2002.

(141) Miller, W. H.; Handy, N. C.; Adams, J. E. *J. Chem. Phys.* **1980**, *72* (1), 99−112.

(142) Palmer, T. *Understanding enzymes*; Ellis Horwood Ltd.: Chichester, West Sussex, England, 1985.

(143) Wolfenden, R.; Snider, M. *Acc. Chem. Res.* **2001**, *34*, 938−945.

(144) Fersht, A. *Structure and Mechanism in Protein Science: A Guide to Enzyme Catalysis and Protein Folding*; W. H. Freeman and Company: New York, 1999.

(145) Kraut, D.; Carroll, K.; Herschlag, D. *Annu. Rev. Biochem.* **2003**, *72*, 517−571.

(146) Kohen, A.; Klinman, J. P. *Acc. Chem. Res.* **1998**, *31*, 397.

(147) Campbell, I. D.; Dobson, C. M.; Williams, R. J. P. *Adv. Chem. Phys.* **1978**, *39*, 55−107.

(148) Gurd, F.; Rothges, T. *Adv. Protein Chem.* **1979**, *33*, 73−165.

(149) Williams, R. *Biol. Rev.* **1981**, *54*, 389−420.

(150) Jardetzky, O. *Acc. Chem. Res.* **1981**, *14*, 291−298.

(151) Levitt, M. *Annu. Rev. Biophys. Bioeng.* **1982**, *11*, 251−271.

(152) Karplys, M.; McCammon, J. *Annu. Rev. Biochem.* **1983**, *53*, 263−300.

(153) Warshel, A.; Parson, W. *Q. Rev. Biophys.* **2001**, *34*, 563−679.

(154) Karplus, M.; McCammon, J. *Nat. Struct. Biol.* **2002**, *9*, 646−652.

(155) Stansfeld, P.; Sansom, M. *Nat. Struct. Biol.* **2011**, *19*, 1562−1572.

(156) Bahnson, B. J.; Colby, T. D.; Chin, J. K.; Goldstein, B. M.; Klinman, J. P. *Proc. Natl. Acad. Sci. U.S.A* **1997**, *94*, 12797.

(157) Garcia-Viloca, M.; Gao, J.; Karplus, M.; Truhlar, D. G. *Science* **2004**, *303*, 5655.

(158) Kamerlin, S.; Mavri, J.; Warshel, A. *FEBS Lett.* **2010**, *584*, 2759−2766.

(159) Rickert, K. W.; Klinman, J. P. *Biochemistry* **1999**, *38*, 12218.

(160) Meyer, M. P.; Klinman, J. P. *Chem. Phys.* **2005**, *319*, 283.

(161) Olsson, M. H. M.; Siegbahn, P. E. M.; Warshel, A. *J. Biol. Inorg. Chem.* **2004**, *9*, 96−99.

(162) Knapp, M. J.; Seebeck, F. P.; Klinman, J. P. *J. Am. Chem. Soc.* **2001**, *123*, 2931.

(163) Samuelsson, B.; Dahlen, S. E.; Lindgren, J. A.; Rouzer, C. A.; Serhan, C. N. *Science* **1987**, *237*, 1171−1176.

(164) Ghosh, J.; Myers, C. E. *Proc. Natl. Acad. Sci. U.S.A.* **1998**, *95*, 13182−13187.

(165) Glickman, M. H.; Wiseman, J. S.; Klinman, J. P. *J. Am. Chem. Soc.* **1994**, *116*, 793−794.

(166) Iyengar, S. S.; Jakowski, J. *J. Chem. Phys.* **2005**, *122*, 114105.

(167) Iyengar, S. S. *Theor. Chem. Acc.* **2006**, *116*, 326.

(168) Jakowski, J.; Sumner, I.; Iyengar, S. S. *J. Chem. Theory Comput.* **2006**, *2*, 1203−1219.

(169) Sumner, I.; Iyengar, S. S. *J. Phys. Chem. A* **2007**, *111*, 10313−10324.

(170) Hatcher, E.; Soudackov, A. V.; Hammes-Schiffer, S. *J. Am. Chem. Soc.* **2007**, *129*, 187.

(171) Hoffman, D. K.; Nayar, N.; Sharafeddin, O. A.; Kouri, D. J. *J. Phys. Chem.* **1991**, *95*, 8299.

(172) Kouri, D. J.; Huang, Y.; Hoffman, D. K. *Phys. Rev. Lett.* **1995**, *75*, 49−52.

(173) Warshel, A.; Weiss, R. M. *J. Am. Chem. Soc.* **1980**, *102*, 6218.

(174) Chang, Y.-T.; Miller, W. H. *J. Phys. Chem.* **1990**, *94*, 5884.

(175) Day, T. J. F.; Soudachov, A. V.; Cuma, M.; Schmidt, U. W.; Voth, G. A. *J. Chem. Phys.* **2002**, *117*, 5839.

(176) Gillan, M. J. *J. Phys. C* **1987**, *20*, 3621.

(177) Voth, G. A.; Chandler, D.; Miller, W. H. *J. Chem. Phys.* **1989**, *91*, 7749.

(178) Warshel, A.; Chu, Z. T. *J. Chem. Phys.* **1990**, *93*, 4003.

(179) Blomberg, M.; Siegbahn, P. *J. Phys. Chem. B* **2001**, *105* (39), 9375−9386.

(180) Roa, L.; Olivares-Renteria, G. A. *Phys. Rev. A* **2006**, *73*, 062327.

(181) Pechen, A.; Il'in, N.; Shuang, F.; Rabitz, H. *Phys. Rev. A* **2006**, *74*, 052102.

(182) Jacobs, K.; Steck, D. A. *Contemp. Phys.* **2006**, *47* (5), 279−303.

(183) Wheeler, J. A., Zurek, W. H., Eds. *Quantum Theory and Measurement*; Princeton University Press: Princeton, NJ, 1983.

(184) Roa, L.; Olivares-Renteria, G. A.; de Guevara, M. L. L.; Delgado, A. *Phys. Rev. A* **2007**, *75*, 014303.

(185) Shuang, F.; Pechen, A.; Ho, T.; Rabitz, H. *J. Chem. Phys.* **2007**, *126*, 134303.

(186) Tannor, D. J.; Rice, S. A. *J. Chem. Phys.* **1985**, *83* (10), 5013−5018.

(187) Brumer, P.; Shapiro, M. *Acc. Chem. Res.* **1989**, *22* (12), 407−413.

(188) Prezhdo, O. V. *Phys. Rev. Lett.* **2000**, *85*, 4413.

(189) Misra, B.; Sudarshan, E. C. G. *J. Math. Phys.* **1977**, *18* (4), 756−763.

(190) Kitano, M. *Phys. Rev. A* **1997**, *56*, 1138−1141.

(191) Minor, W.; Steczko, J.; Stec, B.; Otwinowski, Z.; Bolin, J. T.; Walter, R.; Axelrod, B. *Biochemistry* **1996**, *35*, 10687−10701.

(192) Morris, G. M.; Goodsell, D. S.; Halliday, R.; Huey, R.; Hart, W. E.; Belew, R. K.; Olson, A. J. *J. Comput. Chem.* **1998**, *19*, 1639−1662.

(193) Meyer, M. P.; Tomchick, D. R.; Klinman, J. P. *Proc. Natl. Acad. Sci., U.S.A.* **2008**, *105*, 1146.

(194) Edwards, S.; Soudackov, A.; Hammes-Schiffer, S. *J. Phys. Chem. B* **2010**, *114*, 6653−6660.

(195) Brooks, B.; Bruccoleri, R.; Olafson, B.; States, D.; Swaminathan, S.; Karplus, M. *J. Comput. Chem.* **1983**, *4*, 187−217.

(196) Glickman, M. H.; Klinman, J. P. *Biochemistry* **1995**, *34*, 14077.

(197) Jonsson, T.; Glickman, M. H.; Sun, S. J.; Klinman, J. P. *J. Am. Chem. Soc.* **1996**, *118*, 10319−10320.

(198) Knapp, M. J.; Klinman, J. P. *Eur. J. Biochem.* **2002**, *269*, 3113.

(199) Bowen, W. R.; Lovitt, R. W.; Wright, C. J. *Biotechnol. Lett.* **2000**, *22*, 893−903.

(200) Press, W. H.; Teukolsky, S. A.; Vetterling, W. T.; Flannery, B. P. *Numerical Recipes In C*; Cambridge University Press: New York, 1992.

(201) Romo, T. D.; Clarage, J. B.; Sorensen, D. C.; Phillips, G. N., Jr. *Proteins* **1995**, *22*, 311−321.

(202) Fazal, F. M.; Block, S. M. *Nat. Photonics* **2011**, *5*, 318−321.

(203) Kinney, J. H.; Balooch, M.; Marshall, G. W.; Marshall, S. J. *Arch. Oral Biol.* **1999**, *44*, 813−822.

(204) Fisher, T. E.; Oberhauser, A. F.; Carrion-Vazquez, M.; Marszalek, P. E.; Fernandez, J. M. *Trends Biochem. Sci.* **1999**, *24*, 379−384.

(205) Chicurel, M. E.; Chen, C. S.; Ingber, D. E. *Curr. Opin. Cell Biol.* **1998**, *10*, 232−239.

(206) Radmacher, M.; Fritz, M.; Kacher, C. M.; Cleveland, J. P.; Hansma, P. *Biophys. J.* **1996**, *70*, 556−567.

(207) Wang, M. D.; Yin, H.; Landick, R.; Gelles, J.; Block, S. M. *Biophys. J.* **1997**, *72*, 1335−1346.

(208) Greenleaf, W. J.; Frieda, K. L.; Foster, D. A. N.; Woodside, M. T.; Block, S. M. *Science* **2008**, *319*, 630−633.

(209) Wang, I. S. Y.; Karplus, M. *J. Am. Chem. Soc.* **1973**, *95*, 8160−8164.

(210) Leforestier, C. *J. Chem. Phys.* **1978**, *68*, 4406−4410.

(211) Marx, D.; Hutter, J.; *Modern Methods and Algorithms of Quantum Chemistry*. John Vonneumann Institute For Computing: Julich, Germany, 2000; Chapter Ab Initio Molecular Dynamics: Theory And Implementation, Vol. *1*, pp 301−449.

(212) Bolton, K.; Hase, W. L.; Peslherbe, G. H. *Modern Methods for Multidimensional Dynamics Computation in Chemistry*. World Scientific: Singapore, 1998; Chapter Direct Dynamics of Reactive Systems, p 143.

(213) Schlegel, H. B. *J. Comput. Chem.* **2003**, *24*, 1514−1527.

(214) Swendsen, R. H.; Wang, J. S. *Phys. Rev. Lett.* **1986**, *57*, 2607−2609.

(215) Hansmann, U. H. E. *Chem. Phys. Lett.* **1997**, *281*, 140−150.

(216) Allen, M. P.; Tildsley, D. J. *Computer Simulation of Liquids*; Claredon Press: Oxford, U.K., 1987.